















































properties of the MNPs<sup>20</sup>. Transition metal dopants reported in literature include nickel, copper, barium, zinc and manganese<sup>26-30</sup> with zinc being the most reported dopant<sup>31-35</sup>. This is most likely due to zinc having no effect on the already minimal toxicity of iron oxide nanoparticles used in biomedical applications since it is a health regulatory element in human body cells.

## 2.2 Synthetic Procedures

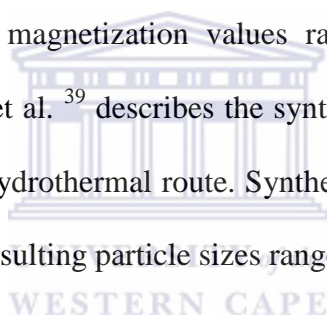
### 2.2.1 Introduction

Reviews by Laurent et al.<sup>17</sup> and Lam et al.<sup>36</sup> describe as many as nine reported synthetic procedures for the preparation of magnetic nanoparticles. These include coprecipitation, hydrothermal, microwave, microemulsion, sonolysis, thermal decomposition, electrospray, sol-gel and flow injection synthesis. It has been reported that the most preferred method for iron oxide magnetic nanoparticle synthesis at both laboratory and industrial levels is the coprecipitation method<sup>17</sup>. This is due to the efficiency and simplicity of technique and the high yield of nanoparticles that can be obtained.

### 2.2.2 Hydrothermal

Due to the broad average particle size distribution of MNPs prepared using the coprecipitation method, new synthetic routes have been devised as a means of yielding particles that are more monodisperse and also have a narrower size distribution. This synthetic route makes use of temperatures of 150 °C and above in a sealed reaction vessel to obtain MNPs from iron salts that have been dissolved in water. The reaction mixture is typically sealed in a teflon-lined autoclave to reach the pressure required for the reaction, and once the reaction time has been achieved, the system is

allowed to cool to room temperature, after which the particles that are obtained are washed and dried as necessary. The reaction temperature, time and choice of iron precursor can be varied to obtain the desired size of MNPs<sup>36</sup>. A review published by Hayashi and Hakuta<sup>37</sup> gives a detailed discussion on the chemistry of hydrothermal synthesis of many metal oxide nanoparticles, including iron oxide nanoparticles with emphasis on the use of supercritical water as a means of controlling the physical and chemical properties of the nanoparticles and gives good insight to the potential of this route. Ge et al.<sup>38</sup> reported the synthesis of MNPs via the hydrothermal route at 135 °C and 2 bar. The nanoparticles obtained were monodisperse had particle sizes ranging from 15 nm to 31 nm(Fig. 1) for the five different reaction conditions reported and saturation magnetization values ranging from 53.3 emu/g to 97.4 emu/g. A report by Cai et al.<sup>39</sup> describes the synthesis of polyethyleneimine-coated MNPs prepared by the hydrothermal route. Synthesis was carried out at 134 °C at 2 bar for 3 hours and the resulting particle sizes ranged from 11.5 nm 18.9 nm.



Though the synthesis of high quality MNPs has been reported for this synthetic route, the somewhat harsh condition required for synthesis, namely the high temperatures and pressure, as well as the need for specialized equipment, make the co-precipitation route a better option due to its simplicity.

### 2.2.3 Thermal decomposition

Another technique that was developed to improve the monodispersity and provide a narrower size distribution is thermal decomposition of iron organic precursors at high temperatures. This technique was first introduced in the late 1970s in which a high boiling solvent such as decalin was used with iron carbonyl ( $\text{Fe}(\text{CO})_5$ ) as the

precursor to produce the nanoparticles <sup>36</sup>. Other iron organic precursors include iron acetylacetonate ( $\text{Fe}(\text{acac})_3$ ) and ( $\text{Fe}(\text{Cup})_3$ ).

Yang et al. <sup>40</sup> reported the synthesis of MNPs via thermal decomposition, using seed crystals and iron (III) acetyl acetonate as precursors, 1,2-hexadecanediol as the solvent and oleic acid and oleyl-amine as the surfactants. The reaction was carried out at 200 °C for 2 hours and then 300 °C for 1 hour. Monodisperse MNPs were obtained with an average particle size of approximately 13.27 nm before ligand exchange with selected poly(amino acids) (Fig. 2). The saturation magnetization values ranged from 36.8 to 73.0 emu/g. Xiao et al. <sup>41</sup> reported on the synthesis of gadolinium-doped iron oxide nanoparticles prepared via thermal decomposition of iron (III) acetyl acetonate and gadolinium (III) acetyl acetonate in diethylene glycol (DEG). The reaction was carried out at 140 °C for 1 hour, followed by a further 8 hours at 200 °C. Highly monodisperse undoped and doped nanoparticles were obtained with average particle sizes of approximately 4.29 nm and 4.74 nm respectively. Saturation magnetization values for the undoped and doped MNPs were 34 emu/g and 25 emu/g respectively.

Narrow size distributions and monodispersed MNPs are obtainable via this route, however, the product cannot be dispersed in aqueous media. This is a requirement for biomedical applications, and would necessitate a ligand exchange step after synthesis, thus making synthesis via co-precipitation a more viable option.

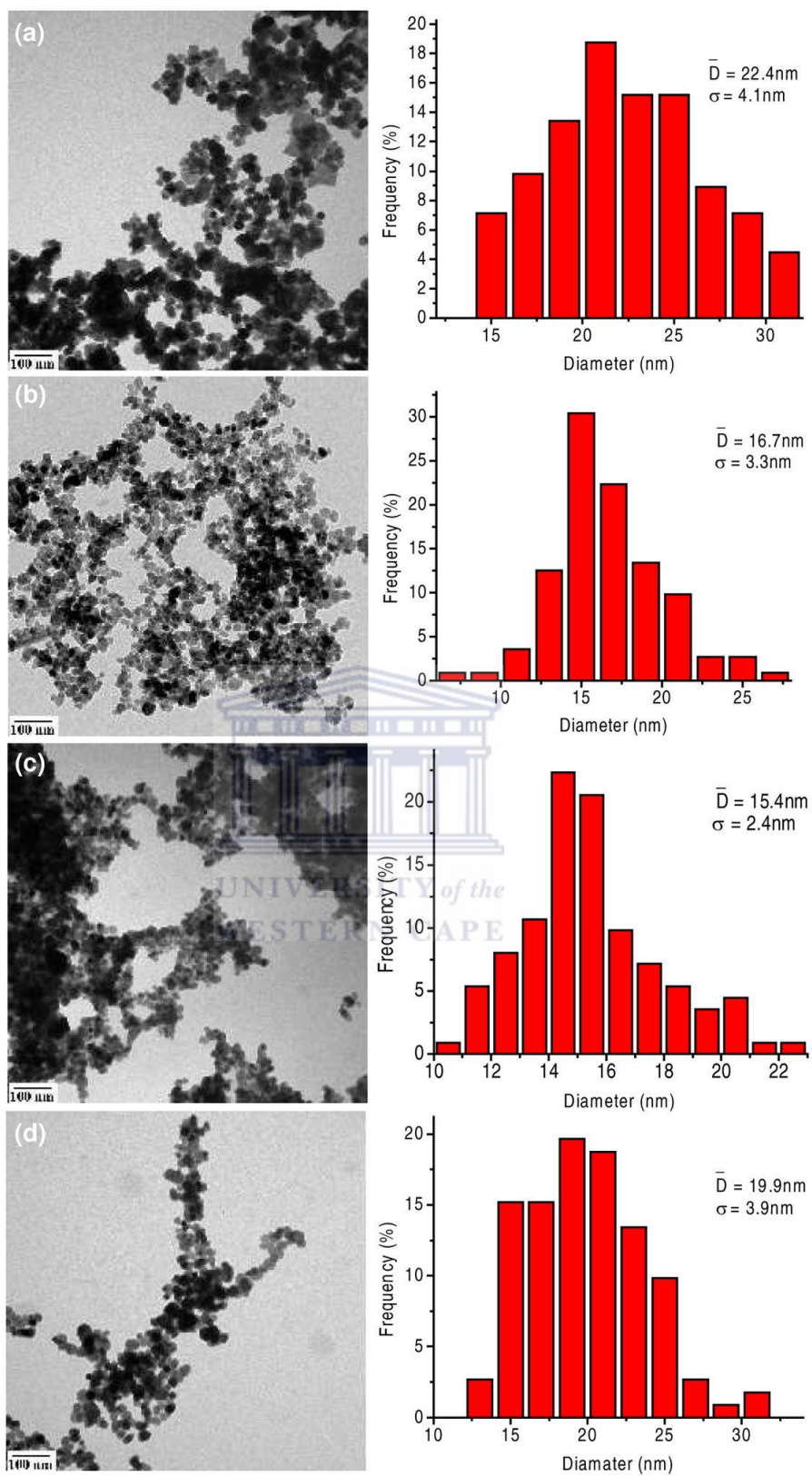


Figure 1: HRTEM micrographs and particle size distributions reported by Ge et al.<sup>27</sup>

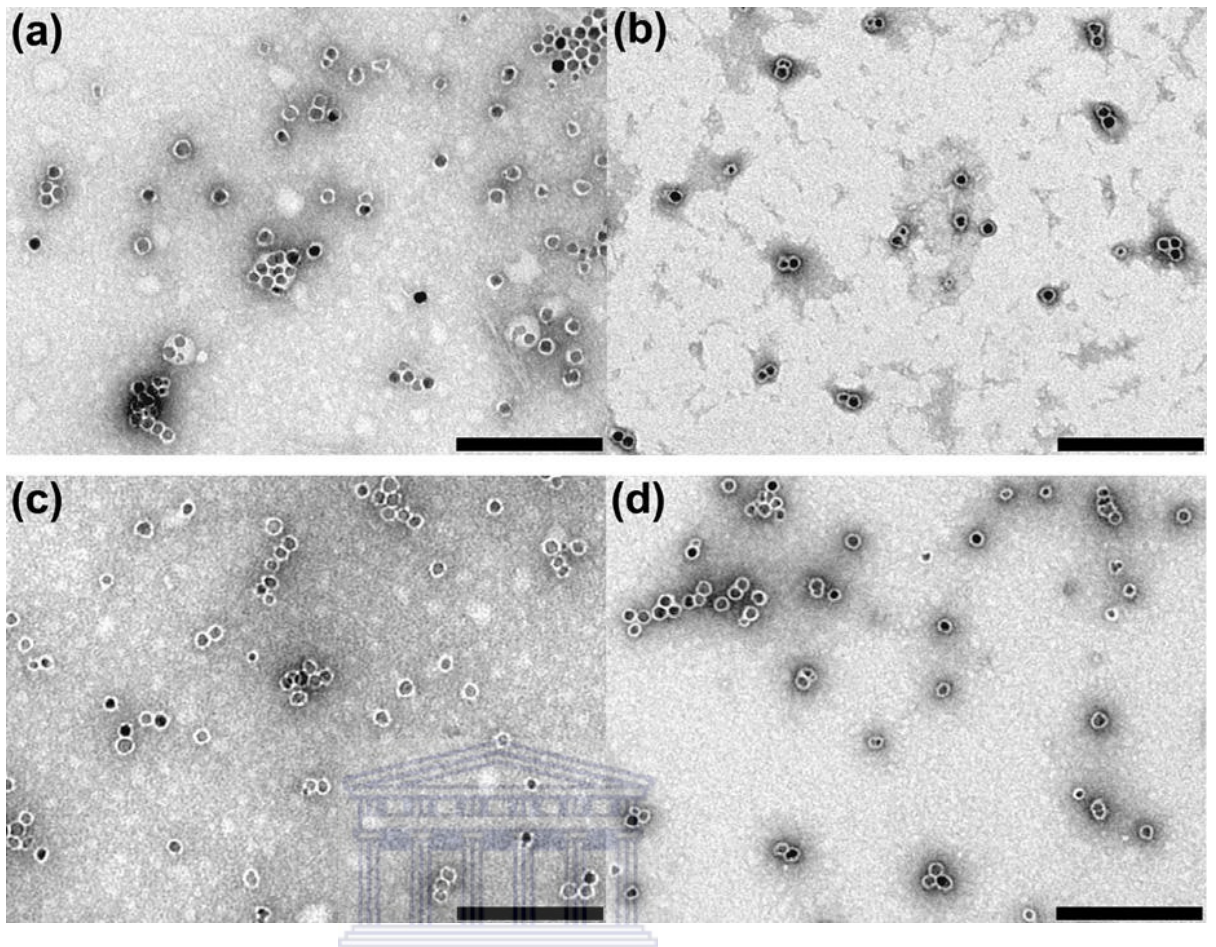
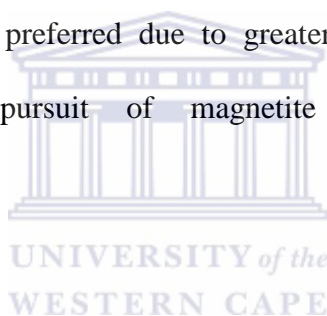


Figure 2: HRTEM images of monodisperse poly(amino acid) coated MNPs reported by Yang et al.<sup>40</sup>. All scale bars are at 200 nm.

#### 2.2.4 Sonication

This method of synthesis involves the formation of a high temperature hot spot created by the quick collapse of cavities that have been produced sonically<sup>17</sup>. Three regions have been identified in this process, i) the interfacial liquid region which lies between the bulk solution and the cavitation bubbles, ii) the inner environment, made up of vaporization and pyrolyzation of water into OH and H radicals due to increased pressures and temperatures, bubbles and iii) the bulk solution which stays at room temperature<sup>25</sup>. This reaction environment induces the formation of iron oxide nanoparticles from ferrous salt precursors<sup>17</sup>. Shen et al.<sup>42</sup> employed this technique to prepare cysteine coated MNPs. Equal amounts of 0.2M L-cysteine and 0.2M iron

sulphate (FeSO<sub>4</sub>) were used as precursors. The reaction took place at room temperature, and the nanoparticles formed within 5 minutes of the addition of the reducing agent. Monodisperse nanoparticles with an average particle size of 15 nm were obtained and the saturation magnetization was reported to be 45 emu/g. The sonochemical synthesis of iron oxide MNPs for the targeted delivery of the drug chitosan has been reported<sup>43</sup>. The loading of the drug was reported to increase with increasing frequency, however, characterization of the MNPs revealed the formation of maghemite and superparamagnetism was not observed. This is due to the oxidation of Fe(II) ions to Fe(III) by hydroxyl radicals produced in the collapse of cavities during synthesis. Based on what has been found in literature, the co-precipitation method is preferred due to greater control of the product formed, specifically in the pursuit of magnetite nanoparticles which display superparamagnetism.



## 2.3 Synthesis via co-precipitation

### 2.3.1 Introduction

The most widely used method of Magnetic nanoparticles in both laboratory and industrial synthesis is the co-precipitation method and involves the chemical co-precipitation of iron salts<sup>44-46</sup>. In this synthetic route magnetite (Fe<sub>3</sub>O<sub>4</sub>) is obtained from an aqueous solution of Fe(III) and Fe(II) salts in a molar ratio of 2:1<sup>17, 42</sup>. The equation of this reaction is as follows:

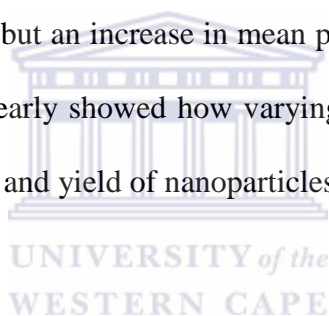


MNPs are obtained if the reaction environment is free of oxygen and non-oxidizing species, and also at a pH in the range of 8-14<sup>47</sup>. This method is also popular due to the large yield of MNPs that is obtained, but its major flaw lies in the broad particle size distribution and this is due to the growth of the nanoparticles only being controlled by kinetic factors<sup>17</sup>.

### 2.3.2 Co-precipitation in literature

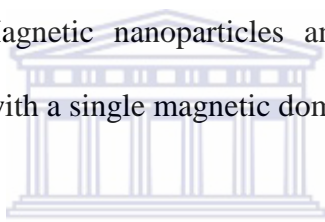
In 1999, a publication by Babes et al.<sup>48</sup> reported the synthesis of iron oxide nanoparticles via the co-precipitation method. Some of the parameters that were varied during the study were the molar ratio of the ferric and ferrous salts, the composition of the basic solution used to initiate the formation and precipitation of the nanoparticles, the temperature, the amount of oxygen present in solution, as well as the stability of the nanoparticles. No surfactant or surface modification was included as part of the study. Transmission electron microscopy (TEM) of the nanoparticles indicated that the use of tetramethylammonium hydroxide (TMAOH) as the base produced large particles of prismatic morphology with an approximate size of 15 nm, while the smaller nanoparticles had more spherical shapes and approximate sizes of around 4 nm. However, combining TMAOH with ammonia yielded nanoparticles which were all angulated spheroids and had a much broader particle size distribution. The temperature was varied between 20 and 65 °C and it was found that the particles obtained showed decreases in size and relaxivity with increasing temperature. A sample of the nanoparticles was exposed to a magnetic field for 24 hours to test the infield stability and it was found that the relaxation rates remained unchanged after the 24 hour period and no induced agglomeration occurred. Results from outfield stability testing showed stability of the nanoparticles

for a minimum of one month. The variation of the ratio of ferric and ferrous salts in solution was limited to a range of 0/10 Fe(II)/Fe(III) and 8/10, and showed that particle size increased and yield ( $67.2 \pm 4.6\%$ ) fell below the average percentage yield of approximately 85% with increasing molar ratio. Ratios of around 0.3 and  $\geq 0.4$  yielded good results with stable nanoparticles being formed, whereas ratios greater than 0.7 gave rise to problems in electromagnetic filtration of the nanoparticles. It was then also deduced that nanoparticles obtained from molar ratios between 0.4 and 0.6 were best for application in MRI. To study the effects of oxygen, the reaction mixture were partially degassed in a nitrogen or argon stream. The yield of nanoparticles decreased from 84.4% to 75.5% when the reaction mixtures were degassed, but an increase in mean particle size increased from 4.3 nm to 5.5 nm. This study clearly showed how varying different parameters can lead to changes in the properties and yield of nanoparticles, however slight the change might be.



In a recent publication, Saraswathy et al. also made use of co-precipitation as a means of MNP synthesis <sup>49</sup>. Anhydrous  $\text{FeCl}_3$  was dissolved in solution with  $\text{FeCl}_2 \cdot \text{H}_2\text{O}$  in a 2:1 molar ratio. The reaction took place at  $80^\circ\text{C}$  and precipitation was initiated with the addition of 1M NaOH to obtain a pH of 12 in the reaction mixture. The reaction was allowed to proceed for 2 hours to allow maximum precipitation of the nanoparticles. Thereafter, the nanoparticles were isolated magnetically, washed and the pH adjusted to allow adequate dispersion in water. The nanoparticles were then mixed with 3% dextran for 6 hours at  $80^\circ\text{C}$ . The coated nanoparticles were then washed with deionized water and centrifuged. The morphology and crystal structure of the nanocrystals were analyzed using high

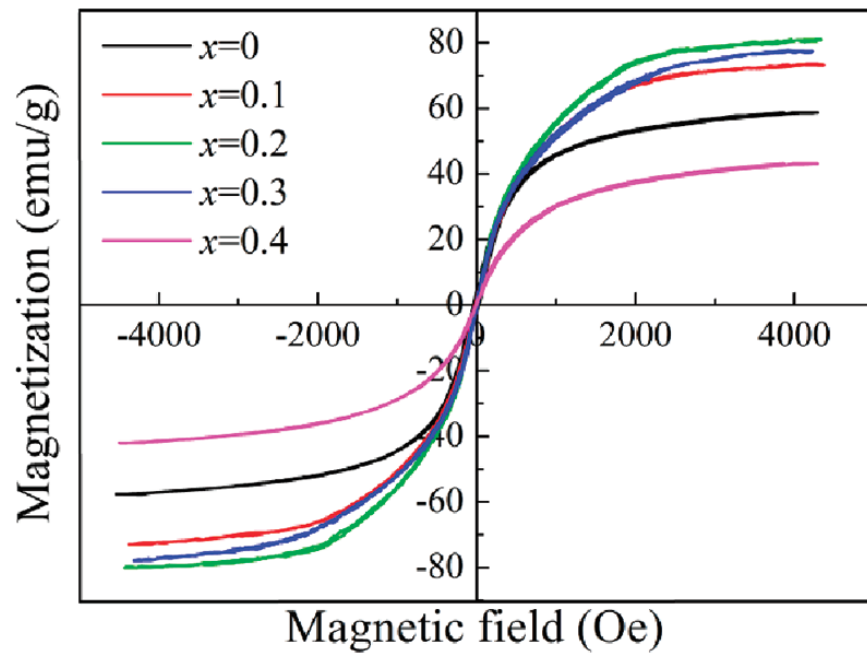
resolution TEM (HRTEM), X-ray diffraction (XRD) and dynamic light scattering (DLS). The micrograph obtained from HRTEM showed particles that were nearly spherical with an average particle size of 12 nm. The dispersity of the particles was attributed to the presence of the dextran, though the image included in the article does not correlate with this observation. The indices from the spectra of XRD analysis confirm that magnetite nanoparticles had formed while the DLS analysis concluded that the hydrodynamic diameter of the nanoparticles was 50 nm. The magnetic properties were analyzed using vibrational sample magnetometer (VSM) and MRI characterization techniques. The zero coercivity of the VSM analysis proves that the nanoparticles are superparamagnetic. The  $M_s$  values varied from 62.7 emu/g for uncapped Magnetic nanoparticles and 45.87 emu/g for the capped Magnetic nanoparticles with a single magnetic domain was identified from this data.



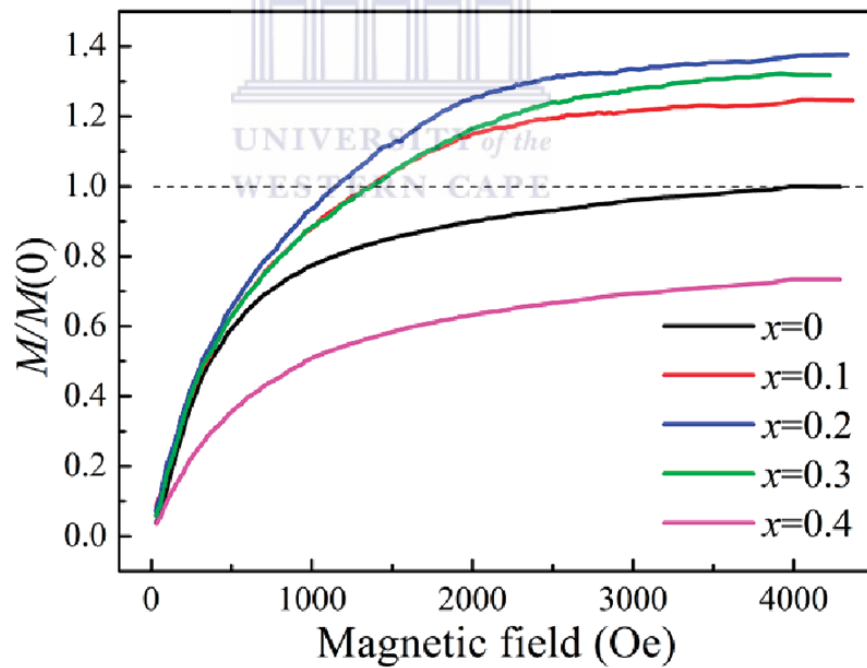
WESTERN CAPE

To date, the inclusion of dopants in the synthesis of magnetic nanoparticles requires a very simple change in the synthetic procedure. Depending on the selected route, the amount of iron precursor is reduced and replaced by the molar equivalent of the selected dopant. Liu et al.<sup>20</sup> reported on the synthesis and characterization of zinc-doped nanoparticles with emphasis on the changes observed in the magnetic properties due to the presence of the dopant (Fig. 3). The coprecipitation route was used to prepare nanoparticles with the formula  $Zn_x Fe_{3-x} O_4$  ( $x=0, 0.1, 0.2, 0.3, 0.4, 0.6, 1.0$ ). Samples of ferrous chloride tetrahydrate ( $FeCl_2 \cdot 4H_2O$ ), ferric chloride hexahydrate ( $FeCl_3 \cdot 6H_2O$ ) and zinc chloride were dissolved in distilled water and stirred under a nitrogen atmosphere to prevent unwanted oxidation of the  $Fe^{2+}$  ions in solution. Three separate surfactants were employed during synthesis, namely polyethylene glycol (PEG), 3-aminopropyltriethoxysilane (APTES) and sodium

dodecyl benzene sulfonate (SDBS). Each surfactant solution was added and vigorously stirred at 500 rpm with the solution heated to 30 °C. After sufficient mixing had taken place, ammonium hydroxide (NH<sub>4</sub>OH) was added dropwise to the reaction mixture to induce formation of the nanoparticles. The pH of the solution was kept at 10 and the reaction allowed to proceed under the same conditions for 1 hour. The temperature was then elevated to 80 °C and the particles allowed to ripen for a further 3 hours. The nanoparticles were then isolated via decantation and the magnetic product washed with distilled water until a pH of 7 was reached. They were further washed thrice with ethanol and dried for 24 hours at 60 °C in a vacuum oven. The resulting product was then ground with a pestle and mortar for characterization. Data collected from vibrating sample magnetometer analysis revealed linear increase in saturation magnetization up to 500 Oe followed by a gradual curved increase up to 2000 Oe and complete saturation at around 4400 Oe. Most importantly was the 37.75% increase in the saturation magnetization in zinc ferrite nanoparticles compared to the pure ferrite nanoparticles. This was observed for zinc ferrite with x=0.2, and is attributed to changes in the crystallite size, lattice spacing and superexchange interaction of atoms within the crystal structure. XRD data confirmed the formation of the face-centered cubic inverse spinel structure inherent in ferrites, with very little difference visible between the undoped and doped nanoparticles. The greatest diffraction intensity was observed for the (311) plane and was used for further studies of the nanocrystal structure. Calculation of average particle size using the Scherrer equation revealed an increase in size up to x=0.2 followed by a decrease and another increase at x=1.0. Since the zinc ferrite with x=1.0 was excluded from VSM characterization, it is clear that x=0.2 is the doping limit for the nanoparticles prepared under the chosen conditions.



(a)



(b)

Figure 3: Saturation magnetization curves for  $Zn_xFe_{3-x}O_4$  MNPs with increasing amounts of zinc dopant reported by Liu et al with (a) the original curves obtained at room temperature and (b) curves at 4400 Oe normalized by  $M(0)$ .<sup>20</sup>

## 2.4 Biomedical Applications

### 2.4.1 Introduction

The biomedical applications of nanotechnologies include use in controlled drug delivery, tissue engineering, biosensors and disease detection, amongst others <sup>50</sup>. At the nanoscale, the two forms of iron oxide, namely magnetite and maghemite, are reported to be the most commonly used materials in biomedicine <sup>51, 52</sup>. These materials are said to have the potential to revolutionize therapeutic techniques and clinical diagnostics <sup>53-57</sup>.

### 2.4.2 MNPs and biomedicine

#### 2.4.2.1 MRI

As mentioned earlier in this work, one of the *in vivo* applications of magnetic nanoparticles is their use as MRI contrast agents for molecular and cell imaging. The distinction between unhealthy and healthy tissue is facilitated by magnetic nanoparticles which behave as a core in the contrast agent <sup>52</sup>. Saraswathy et al made use of dextran coated magnetic nanoparticles as a contrast agent for the MRI of liver fibrosis <sup>49</sup>.

#### 2.4.2.2 Drug delivery

For more than 30 years, MNPs have been developed as next generation components in drug delivery due to their functionality at both cellular and molecular levels <sup>58,59</sup>. The aim of this technique is to direct the drug to the exact location of the disease and deliver it without having any negative effects on the surrounding healthy tissue <sup>60</sup>. Wang et al. <sup>61</sup> reported the successful preparation of block co-polymer coated MNPs

for the delivery of curcumin. The synthesis of block co-polymer coated MNPs for delivery of doxorubicin <sup>62</sup> has also been reported.

### 2.4.3 MNPs and breast cancer research

#### 2.4.3.1 Breast cancer cell separation

Another biomedical application is the use magnetic nanoparticles for the targeting and separation of cells from biological mixtures. It has been reported that before tumors are detected in the body, circulating tumor cells (CTCs) can be found in the blood stream <sup>63, 64</sup>. The challenge arises in from the fact that blood contains  $2.5-4 \times 10^8$  platelets,  $3-10 \times 10^6$  white blood cells and  $3-9 \times 10^9$  red blood cells per milliliter, whereas CTCs are only found in the range of 0-50 per milliliter of blood <sup>56</sup>. Xu et al. <sup>67</sup> reported the cell separation capabilities of MNPs that were prepared via thermal decomposition and were found to be  $27 \pm 5$  nm in size. The hydrophobic nanoparticles were made hydrophilic through the addition of a amphiphilic polymer over the hydrophobic surfactant, thus increasing the overall size to 33 nm. Carboxyl groups present in the surfactant allowed for bioconjugation with anti-HER2 via a covalent bond with an amine group in the antibody, which facilitates the targeting of the HER2 protein receptor tyrosine kinase that is over expressed on the surface of SK-BR3 breast cancer cells. The Dulbecco's phosphate (DPBS), DPBS + bovine serum albumin (BSA), RPMI-1640, RPMI-1640 medium supplemented with 10% heat-inactivated fetal bovine serum(FBS) and 1% streptomycin/penicillin, and human plasma were used in testing the stability of the functionalized nanoparticles in biological media. Tests showed that the nanoparticles remained stable in all the above mentioned media, except RBPMI-1640 in which the nanoparticles precipitated. The specificity of the functionalized nanoparticles was tested in a buffer

solution after staining with Prussian blue. TEM was used to examine the activity of the nanoparticles after adding them to the cancer cell culture and it was found that the nanoparticles were highly attracted to the surface of the cell, and some were even drawn into the cancer cells via the endocytotic pathway and trapped within cellular vesicles (Fig. 4). Another study was carried out to examine the nanoparticle activity when exposed to the whole isolated HER2 receptor. Sodium dodecyl sulphate polyacrylamide gel electrophoresis (SDS-PAGE) results showed that nanoparticles that were not conjugated to the antibody had no attraction to the HER2 receptor. However, the conjugated nanoparticles that were conjugated to the receptor caused lagging progression through the gel when combined with the SK-BR3 cell lysate and increasing concentrations of the isolated receptor. This further proved the efficiency and specificity exhibited by the conjugated nanoparticles. Finally, the nanoparticles were tested in samples of whole female human blood that had been mixed with the SK-BR3 cancer cells. The cell count for the commercial female human blood showed a total cell count of  $4.2 \times 10^7$  cells/mL with the red blood cell content measured to  $4.4 \times 10^9$  cells/mL. 300 SK-BR3 cells were stained with 5-chloromethylfluorescein diacetate (CMFDA) and mixed with 1 mL of the whole blood to attain an approximate cancer cell to blood cell ratio of 1:10 000 000. The nanoparticles were introduced to the mixture and a permanent magnet was used to attract the cancer cells and nanoparticles out of the mixture. A sample of the conjugated nanoparticles and cancer cells were then examined under a microscope and the number of cancer cells was determined due to the larger size and difference in colouration. It was reported that a recover of up to 86% was observed with an average of 73.6% for all the tests performed. This proved how effective the nanoparticle systems were compared to current methods of cell separation.

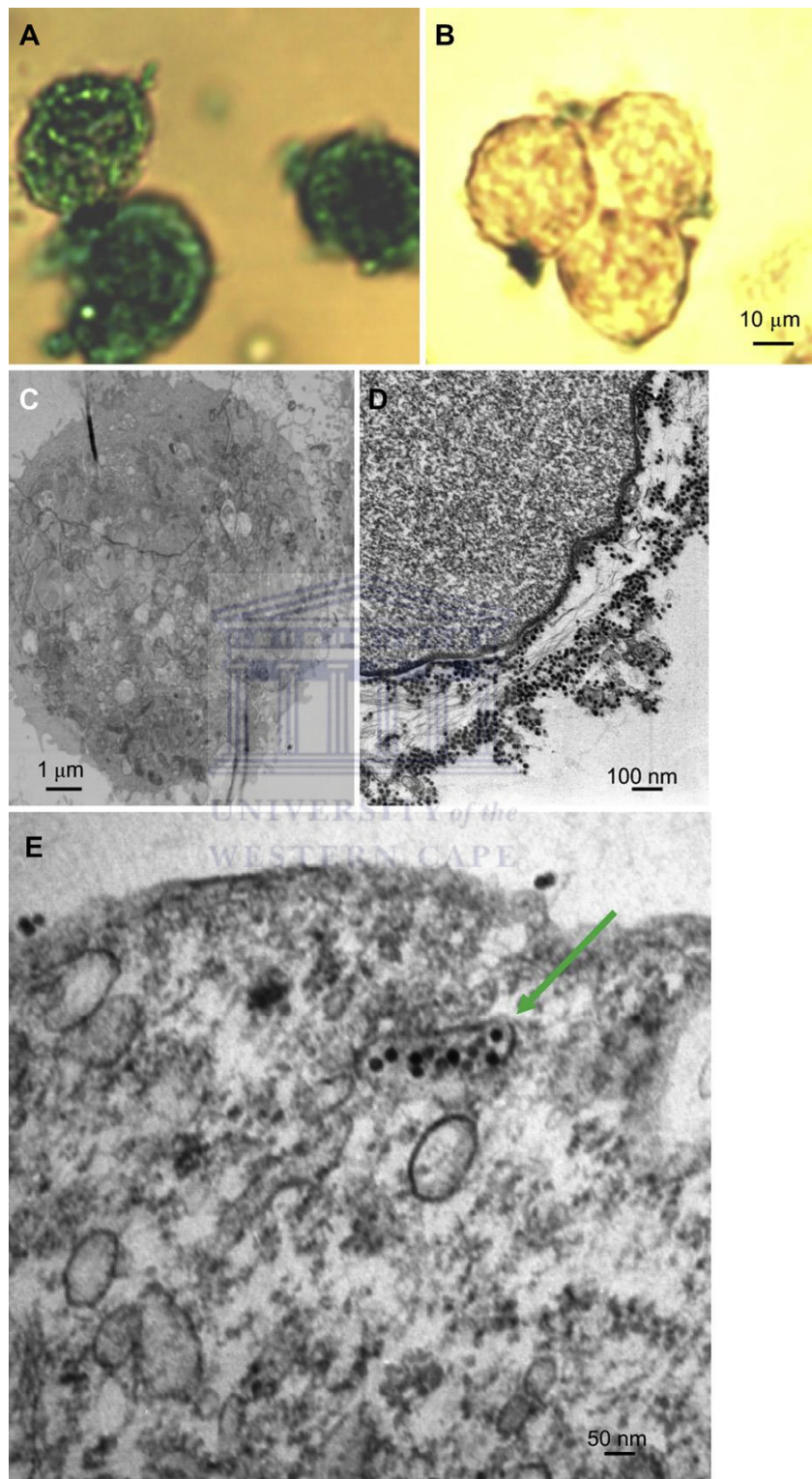


Figure 4: TEM images reported by Xu et al<sup>67</sup> showing cancer cells stained with Prussian blue A) exposed to antibody-functionalized MNPs, B) exposed to MNPs with carboxyl functionalization, C) low magnification of cell section, D) partial magnification showing

exposure to antibody-functionalized MNPs and E) showing evidence of cellular uptake of antibody-functionalized MNPs.

#### 2.4.3.2 Breast cancer drug delivery

One of the greatest problems in cancer therapy via chemotherapy methods is the lack of specificity in the targeting of tumor cells. Research work reported by Marcu et al<sup>68</sup> was based on this, in an attempt to overcome this problem. MNPs were prepared via laser pyrolysis of vapour precursors and coated with the VB1 drug. Monodispersed MNPs with an average particle size of 8-10 nm were reported in this study. The targeted cell line selected was that of human breast adenocarcinoma cancer, MCF-7. Cellular uptake of the drug coated nanoparticles was better in comparison to pure iron oxide MNPs of 20 nm due to the smaller size. Tests with free VB1 showed a more rapid decrease in cellular impedance and the appearance of apoptotic vesicles in the cancer cells compared to the coated nanoparticles, with the time taken reported as 10 hours for the free VB1 and a much longer time period for the coated MNPs (data not reported). This was attributed to the different endocytotic pathway taken by the coated MNPs when passing through the plasma membrane.

#### 2.4.3.3 Doped MNPs and breast cancer

MNPs doped with manganese and zinc to yield particles with the formula  $Mn_{0.24}Zn_{0.76}Fe_2O_4$  were reported by Latorre-Esteves et al<sup>69</sup>. The co-precipitation route was used and nanoparticles with an average size of 15 nm were obtained and the superparamagnetic nature of the nanoparticles was also confirmed. Tests on the MCF-7 cell line showed no changes in the cell viability, therefore confirming that the biocompatibility of the MNPs was maintained after doping with magnesium and zinc.

## 2.5 Conclusion

The literature discussed within this chapter is only a small fraction of the research that has been reported on the synthesis, characterization and applications of MNPs. Strong evidence is given for the use of MNPs in biomedical applications as well as the enhancing effects exhibited by the inclusion of dopants during synthesis. It is upon this foundation that the work discussed in the following chapters is built with the aim of preparing superparamagnetic zinc-doped iron oxide nanoparticles that are suitable for application in biomedicine.

## 2.6 References

1. A. Figuerola, R. D. Corato, L. Manna, T. Pellegrino, (2010). *Pharmacological Research*, 62, 126–143.
2. M. Mahmoudi, S. Sant, B. Wang, S. Laurent, T. & Sen, (2011) *Advanced Drug Delivery Reviews*, 63,24–46.
3. G. Goloverda, B. Jackson, C. Kidd, V. Kolesnichenko, (2009) *Journal of Magnetism and Magnetic Materials*, 321, 1372–1376.
4. C. Qin, C. Li, Y. Hu, J. Shen, M. Ye, (2009) *Colloids and Surfaces A: Physicochemical and Engineering Aspects*, 336, 130–134.
5. H. G. Cha, C. W. Kim,. S. W. Kang, B. K. Kim, Y. S. Kang, (2010) *Journal of Physical Chemistry C*, 114, 9802–9807.
6. X. Li, B. Zhang, C. Ju, X. Han, Y. Du, P. Xu, (2011) *Journal of Physical Chemistry C*, 115, 12350–12357.
7. Hu, A.; Yee, G. T.; Lin, W. J., (2005) *American Chemical Society*, 127,12486–12487.
8. J. Meng; G. Yang, L. Yan, X. Wang, (2005) *Dyes and Pigments*, 66, 109–113.

9. Z.M. Cui, L.Y. Jiang, W.G. Song, Y.G. Guo, (2009) *Chemistry of Materials*, 21, 1162–1166.
10. H. Parham, B. Zargar, R. Shiralipour, (2012), *Journal of Hazardous Materials*, 205-206, 94–100.
11. H. Parham, B. Zargar, M. Rezazadeh, (2012) *Materials Science and Engineering: C*, 32, 2109–2114.
12. H. Xu, Z.P. Aguilar, L. Yang, M. Kuang, H. Duan, Y. Xiong, H. Wei, A. Wang, (2011) *Biomaterials*, 32, 9758–9765.
13. H. Vu-Quang, M. Yoo, H. Jeong, H. Lee, M. Muthiah, J.H. Rhee, I. Park, J. Lee, C. Cho, Y. Jeong (2011), *Acta Biomaterialia*, 7, 3935–3945.
14. K. Andreas, R. Georgieva, M. Ladwig, S. Mueller, M. Notter, M. Sittige, J. Ringe, (2012) *Biomaterials*, 33,4515–4525.
15. T.K. Jain, S.P. Foy, B. Erokwu, S. Dimitrijevic, C. A. Flask, V. & Labhasetwar, (2009) *Biomaterials*, 30, 6748–6756.
16. M.G. Krukemeyer, V. Krenn, M. Jakobs, W. Wagner, (2012) *Journal of Surgical Research*, 175, 35–43.
17. S. Laurent, D. Forge, M. Port, A. Roch, C. Robic, L. Vander Elst, R.N. Muller, (2008) *Chemical Reviews*, 108, 2064–2110.
18. S. Xuan, Y. X. J. Wang, J.C. Yu, K. Cham Fai Leung, (2009) *Chemistry of Materials*, 21, 5079–5087.
19. Kittel, (1946) *C. Physical Review*, 70, 965–971.
20. J. Liu, Y. Bin, and M. Matsuo, (2012) *Journal of Physical Chemistry C*, 116, 134–143
21. D.L. Leslie-Pelecky, R.D. Rieke, (1996) *Chemistry of Materials*, 8, 1770–1783.

22. Q. Song, Z.J. Zhang, (2006) *Journal of Physical Chemistry B*, 110, 11205–11209.
23. Y. Pu, X. Tao, X. Zeng, Y. Le, J.-F. Chen, (2010) *Journal of Magnetism and Magnetic Materials*, 322, 1985–1990.
24. A.K. Gupta, M. Gupta, (2005) *Biomaterials*, 26, 3995–4021.
25. P. Kristan, V. Chlan, H. Stepankova, R. Reznicek, P. Görnert, P. Payer, (2014) *Acta Physica Polonica A*, 126, 138-139.
26. C. Yao, Q. Zeng, G.F. Goya, T. Torres, J. Liu, H. Wu, M. Ge, Y. Zeng, Y. Wang, J.Z. Jiang, (2007) *Journal of Physical Chemistry C*, 111, 12274-12278.
27. G.V.M. Jacintho, A.G. Brolo, P. Corio, P.A.Z. Suarez, J.C. Rubim, (2009) *Journal of Physical Chemistry C*, 113, 7684-7691.
28. Q. He, H.Z. Wang, G.H. Wen, Y. Sun, B.J. Yao, (2009) *Journal of Alloys and Compounds*, 486, 246-249.
29. L. Li, G. Li, R.L. Smith, H. Inomata, (2000) *Chemistry of Materials*, 12, 3705-3714.
30. M. Mozaffari, S. Manouchehri, M.H. Yousefi, J. Amighian, (2010) *Journal of Magnetism and Magnetic Materials*, 322, 383-388.
31. R. Gupta, A.K. Sood, P. Metcalf, J.M. Honing, (2002) *Physical Review B*, 65, 104430.
32. M. Wen, Q. Li, Y. Li, *Journal of Electron Spectroscopy Related Phenomena*, 153, 65-70.
33. C.M. Srivastava, S.N. Shringi, R.G. Srivastava, N.G. Nanadikar, (1976) *Physical Review*, 14, 2041.
34. C.M. Srivastava, S.N. Shringi, R.G. Srivastava (1976) *Physical Review B*, 14 2041

35. Z.L. Lu, L.Y. Lv, J.M. Zhu, S.D. Li, X.C. Liu, W.Q. Zou, F.M. Zhang, Y.W. Du, (2006) *Solid State Communications*, 137, 528-532.
36. T. Lam, P. Pouliot, P.K. Avti, F. Lesage, A.K. Kakkar, (2013) *Advances in Colloid and Interface Science*, 199–200, 95–113
37. H. Hayashi, Y. Hakuta, (2010) *Materials*, 3, 3794-3817
38. S. Ge, X. Shi, K. Sun, C. Li1, J.R. Baker Jr., M.M. Banaszak Holl, B.G. Orr, (2009) *Journal of Physical Chemistry C Nanomaterial Interfaces.*, 113(31): 13593–13599.
39. Hongdong Cai, Xiao An, Jun Cui, Jingchao Li, Shihui Wen, Kangan Li, Mingwu Shen, Linfeng Zheng, Guixiang Zhang, Xiangyang Shi, (2013) *American Chemical Society Applied Material Interfaces*, 5, 1722–1731.
40. H. Yang, C.W. Park, T. Ahn, B. Jung, B. Seo, J. Park, J. Kim, (2013) *Journal of Colloid and Interface Science*, 391, 158–167.
41. N. Xiao, W. Gu, H. Wang, Y. Deng, X. Shi, L. Ye, (2014) *Journal of Colloid and Interface Science* 417 159–165
42. X. Shena, Q. Wangb, W. Chen, Y. Pang, (2014) *Applied Surface Science*, 317, 1028–1034.
43. R. Dolores, S. Raquel, G. Adianez, (2015) *Ultrasonics Sonochemistry*, 23, 391-398.
44. S.-J.Lee, J.-R. Jeong, S.-C. Shin, J.-C. Kim, J.-D. Kim, (2004) *Journal of Magnetism and Magnetic Materials*, 282, 147-150.
45. Y.-K. Sun, M. Ma, Y. Zhang, N. Gu, (2004) *Colloids and Surfaces A*, 245, 15-19.
46. I. Martinez-Mera, M.E. Espinosa, R. Perez-Hernandez, J. Arenas-Alatorre, (2007) *Materials Letters*, 61, 4447–4451.

47. J.P. Jolivet, C. Chaneac, E. Tronc, (2004) *Chemical Communications*, 5, 481.
48. L. Babes, B. Denizot, G. Tanguy, J.J. Le Jeune, P. Jallet, (1999) *Journal of Colloid and Interface Science*, 212, 474–482
49. A. Saraswathya, S. S. Nazeera, N. Nimia, S. Arumugamb, S. J. Shenoyc, R. S. Jayasreea, (2014) *Carbohydrate Polymers*, 101, 760– 768.
50. J. Chomouckaa, J. Drbohlavovaa, D. Huskab, V. Adamb, R. Kizekb, J. Hubalek, (2010) *Pharmacological Research*, 62, 144–149
51. P. Majewski, B. Thierry, (2007) *Critical Reviews in Solid State and Material Sciences* 32 (3-4) 203-215.
52. Z.P. Xu, Q.H. Zeng, G.Q. Lu, A.B. Yu, (2006) *Chemical Engineering Science*, 61 (3), 1027-1040.
53. B. Mishra, B.B. Patel, S. Tiwari (2009) *Nanomedicine: Nanotechnology, biology and medicine*, 6 (1), 9-24
54. W.H. Suh, K.S. Suslick, G.D. Stucky, Y.H. Suh, (2009) *Progress in Neurobiology*, 87, 133–70.
55. P. Stepp, F. Thomas, P.R. Lockman, H. Chen, A.J. Rosengart, (2009) *Journal of Magnetism Magnetic Materials* 321, 1591–1593.
56. Mailander V, Landfester K., (2009) *Biomacromolecules*, 10, 2379–2400.
57. V. Kral, J. Sotola, P. Neuwirth, Z. Kejik, K. Zaruba, P. Martasek, (2006) *Chemicke Listy*, 100, 4–9.
58. S.C. McBain, H.H.P Yiu, J. Dobson, (2008) *International Journal Nanomedicine*, 3, 169–180.
59. M. Shinkai, (2002) *Journal of Bioscience and Bioengineering*, 94, 606–613.
60. J. Chomouckaa, J. Drbohlavovaa, D. Huskab, V. Adamb, R. Kizekb, J. Hubalek, (2010) *Pharmacological Research*, 62, 144–149.

61. N. Wang, Y. Guan, L. Yang, L. Jia, X. Wei, H. Liu, C. Guo, (2013) *Journal of Colloid and Interface Science*, 395, 50–57.
62. M. Hałupka-Bryl, K. Asaic, S. Thangavel, M. Bednarowicz, R. Krzymiński, Y. Nagasaki, (2014) *Colloids and Surfaces B: Biointerfaces*, 118, 140–147.
63. A. S. Teja, P. Koh, (2009) *Progress in Crystal Growth and Characterization of Materials*, 55, 22-45.
64. J.J. Gaforio, M.J. Serrano, P. Sanchez-Rovira, A. Sirvent, M. Delgado-Rodriguez, M. Campos, N. del la Torre, I. Algarra, R Dueñas, A. Lozano (2003) *International Journal of Cancer*, 107, 984-990.
65. J.Y. Pierga, C. Bonneton, A. Vincent-Salomon, P. de Cremoux, C. Nos, N. Blin, P. Pouillart, J.P. Thiery, H. Magdelénat, (2004) *Clinical Cancer Research*, 10, 1392-1400.
66. W.J. Allard, J. Matera, M.C. Miller, M. Repollet, M.C. Connelly, C. Rao, A.G. Tibbe, J.W. Uhr, L.W. Terstappen, (2004) *Clinical Cancer Research*, 10, 6897-6904.
67. H. Xu, Z. P. Aguilar, L. Yang, M. Kuang, H. Duan, Y. Xiong, H. Wei, A. Wang, (2011) *Biomaterials*, 32, 9758-9765.
68. A. Marcu, S. Pop, F. Dumitrache, M. Mocanu, C.M. Niculite, M. Gherghiceanu, C.P. Lungu, C. Fleaca, R. Ianchis, A. Barbut, C. Grigoriu, I. Morjan, (2013) *Applied Surface Science*, 281, 60–65.
69. M. Latorre-Esteves, A. Cortés, M. Torres-Lugo, C. Rinaldi, *Journal of Magnetism and Magnetic Materials* 321 (2009) 3061–3066.

## Chapter 3

### Chapter Overview

Chapter 3 gives a discussion of the methodology employed to prepared zinc-doped MNPs and the characterization techniques used to study the physicochemical properties of the as-prepared nanoparticles.

### 3. Methodology

#### 3.1 Chemicals

Anhydrous iron (III) chloride ( $\text{FeCl}_3$ ), iron (II) sulphate ( $\text{FeSO}_4$ ), 25% ammonium hydroxide ( $\text{NH}_4\text{OH}$ ) and polyethylene glycol (PEG) were used. 3-phosphonopropionic acid (3-PPA) was purchased from Sigma Aldrich (South Africa). All reagents were of analytical grade. Preparation of all MNPs took place in the Nanomaterials and Organometallics Research Laboratory at the University of the Western Cape.

#### 3.2 Synthesis

##### 3.2.1 Procedure

A novel synthetic procedure for the synthesis of zinc doped MNPs is presented. Preliminary experiments were carried out to test the co-precipitation method. The ferric and ferrous salts mentioned above were dissolved in deionized water with a known amount of PEG in a three neck round bottomed flask and flushed with nitrogen to prevent oxidation of the Fe(II) ions to Fe(III). The brown solution was heated to 50 °C, at which point a known amount of 25%  $\text{NH}_4\text{OH}$  was slowly injected

into the flask to induce the formation of the nanoparticles. The product was left to ripen for two hours after which it was isolated via magnetic decantation and taken for characterization.

Doped Fe<sub>3</sub>O<sub>4</sub> nanoparticles with the formula Zn<sub>x</sub>Fe<sub>3-x</sub>O<sub>4</sub> ( $x = 0, 0.1, 0.2, 0.3, 0.4$ ) were prepared via the co-precipitation method. The formation of the doped MNPs is represented by the following balanced chemical equation:



The amount of dopant added for each value of  $x$  was controlled in such a manner as to keep the ratio of trivalent and divalent metal cations at 2:1. To improve dispersibility, 3-phosphonopropionic acid (3-PPA) was introduced as a capping agent. In a typical synthesis of doped MNPs, weighed samples of anhydrous ferric chloride (FeCl<sub>3</sub>), ferrous sulphate (FeSO<sub>4</sub>) and hydrated zinc chloride (ZnCl<sub>2</sub>·4H<sub>2</sub>O) were dissolved in deionized water and stirred magnetically to obtain a homogenous mixture. The flask was flushed with nitrogen and heated to 40 °C and the reaction mixture stirred at 400rpm for the duration of the reaction. A known volume of 25% ammonium hydroxide (NH<sub>4</sub>OH) was slowly injected into the flask to induce co-precipitation and formation of the nanoparticles. After ripening for 30 minutes, the 3-PPA that was dissolved in water was injected into the reaction mixture. This was done to prevent an unwanted reaction between the NH<sub>4</sub>OH and the 3-PPA. The nanoparticles were then allowed to ripen for a further 30 minutes before isolation and purification.

### 3.2.2 Isolation and purification

The as-prepared zinc ferrite nanoparticles were isolated via magnetic decantation. The precipitate solid product was washed with deionized water and ethanol to remove excess  $\text{NH}_4\text{OH}$  and 3-PPA. The supernatant liquid obtained from magnetic decantation contained both the reducing and capping agents and was disposed of as toxic waste.

### 3.2.3 Sample preparation

#### 3.2.3.1 HRTEM and EDS

Samples were dispersed in deionized water for analysis. The samples were then deposited onto the required platform for characterization.

#### 3.2.3.2 XRD, FTIR, TGA, and SQUID

Samples were dried in a vacuum oven at  $60\text{ }^\circ\text{C}$  for 24 to 36 hours. Once sufficient drying had taken place, a pestle and mortar was used to grind the solid material into a fine powder. Samples were divided, labeled and taken or sent for analysis.

### 3.3 Characterization

#### 3.3.1 HRTEM

High resolution transmission electron microscopy (HRTEM) was used to characterize the morphology, size and dispersion of the nanoparticles. In this technique, a high energy electron beam is generated from an electron source and focused onto the sample which is deposited onto a small metal grid, as seen in Fig. 5. The electron beam is necessary to observe materials with morphological features in the nanoscale and is focused onto a point on the sample grid by magnets arranged

along the path of the beam. As the name of this technique suggests, the beam is transmitted through the sample, and changes in the energy of the electrons is detected and converted by sophisticated software to generate an image of the material. For the characterization of the  $Zn_xFe_{3-x}O_4$  nanoparticles ( $x=0, 0.1, 0.2, 0.3, 0.4$ ), samples were dispersed in deionized water and dropped onto a copper grid. The grid was allowed to dry in air before being inserted into the microscope. An FEI Tecnai<sup>TM</sup> F30ST field emission gun transmission electron microscope (FEG-TEM), operated at an accelerating voltage of 200 kV in bright-field mode was used in this study.

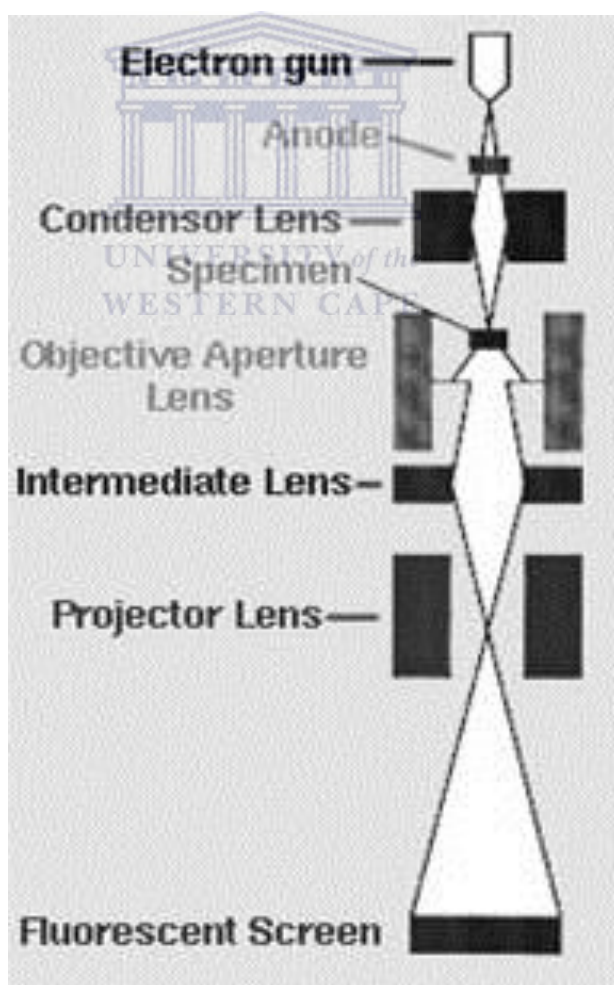


Figure 5: Schematic of the components of a standard HRTEM instrument <sup>1</sup>.

### 3.3.2. XRD

The identification of the crystal structure of a material is important for confirming that the correct material has been synthesized. X-ray diffraction spectroscopy is a technique in which an organic or inorganic sample<sup>2</sup> is exposed to monochromatic X-rays generated from a cathode ray tube. As the X-rays enter the sample, they encounter the atoms arranged within the crystal structure, and are diffracted out of the sample material as seen in Fig 6.

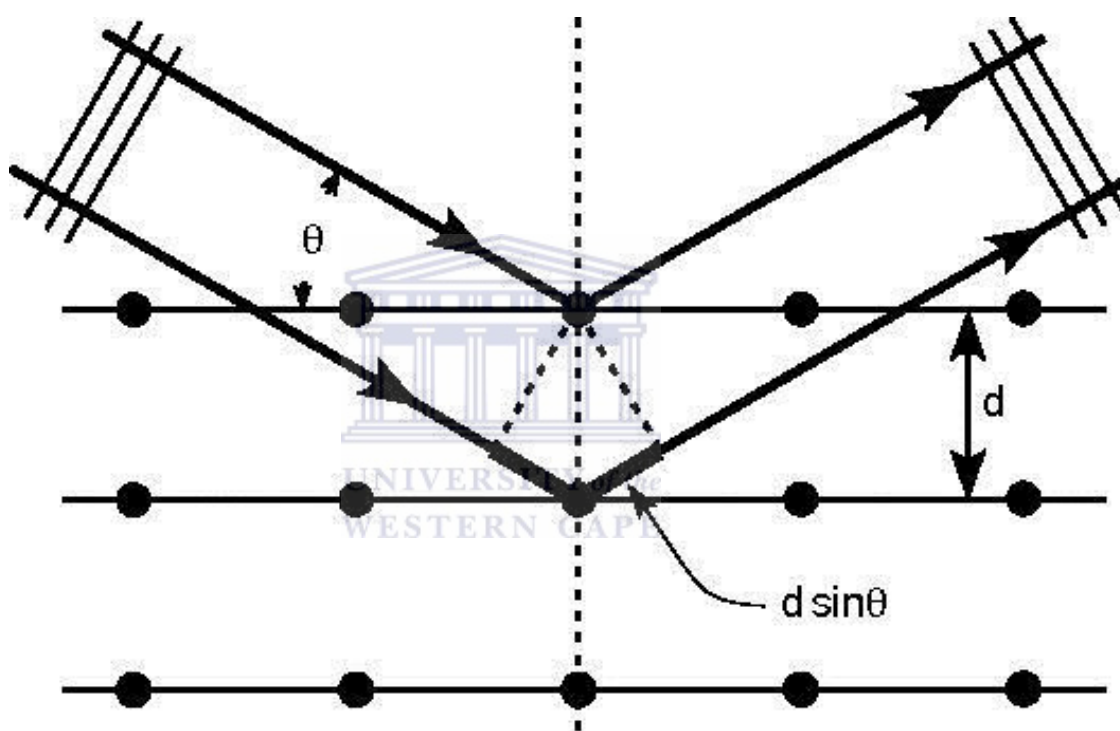


Figure 6: A schematic diagram showing X-rays interacting with a crystal structure in XRD analysis<sup>3</sup>.

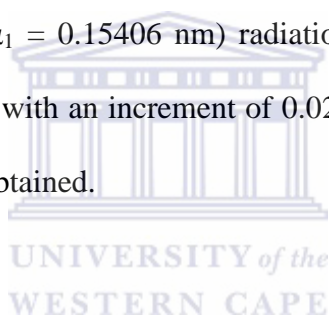
Bragg's Law shows the relationship between the wavelength of the X-ray,  $\lambda$  (nm), the lattice spacing,  $d$  (nm) and the diffraction angle,  $\theta$  ( $^{\circ}$ ):

$$n\lambda = 2d\sin\theta \quad (3)$$

where  $n$  is the order.

The diffracted X-rays are detected by the instrument and software is used to convert the data into spectra. Peaks that appear in the spectrum can be attributed to the X-rays interacting with specific domains of the crystal structure and can be compared to fingerprints in the identification and confirmation of materials. One advantage of this technique is that samples are not lost or destroyed and can be taken collected and used elsewhere after characterization.

For the determination of the crystal structure of the undoped and doped nanoparticles presented in this work, samples in a dry, powdered form were characterized in a Bruker AXS D8 Advance Diffractometer (Germany) fitted with a PSD Vantec-1 detector. A Cu-K $\alpha$  ( $\lambda K\alpha_1 = 0.15406$  nm) radiation source was used. The selected range for  $2\theta$  was 20-70° with an increment of 0.02°. OriginPro 8 software was used to convert the raw data obtained.



### 3.3.3 EDS

Elemental analysis of samples confirms the presence of the desired elements within the sample and also reveals the presence of any impurities. This technique is performed on samples after characterization with HRTEM. Upon exposure to the electron beam, the electrons within the sample are excited to a higher energy level, and release X-rays as they return to the ground state<sup>4</sup>. The wavelength of each X-ray is unique to the element from which it was emitted, and this is then detected and used to identify the elements present in the sample and also yields data on the percentage abundance of the elements within the sample. The EDS spectra were collected with a liquid nitrogen cooled EDAX SiLi detector. Each spectrum was collected for 30 seconds.

### 3.3.4 FTIR

The use of surfactants in nanoparticle synthesis requires the use of a technique to confirm that the surfactant is indeed linked in some way to the surface of the nanoparticle. In FTIR, the sample is placed between the beam splitter (interferometer) and the detector, as seen in Fig. 7. An interferogram, or spectrum, is generated by subtracting the spectrum of the sample from that of the continuous light source. An interferogram of the solvent is collected first, followed by the analyte dissolved in the solvent as required. The spectrum of the sample that is generated by the instrument is the result of the division of the second interferogram by the first<sup>5</sup>. To determine whether 3-PPA was bonded to the surface of the nanoparticle a Perkin Elmer Spectrum2 was used. Both the capped and uncapped nanoparticles of  $x=0.2$  were characterized by grinding the dry sample with KBr and compressing the powder to form a pellet.

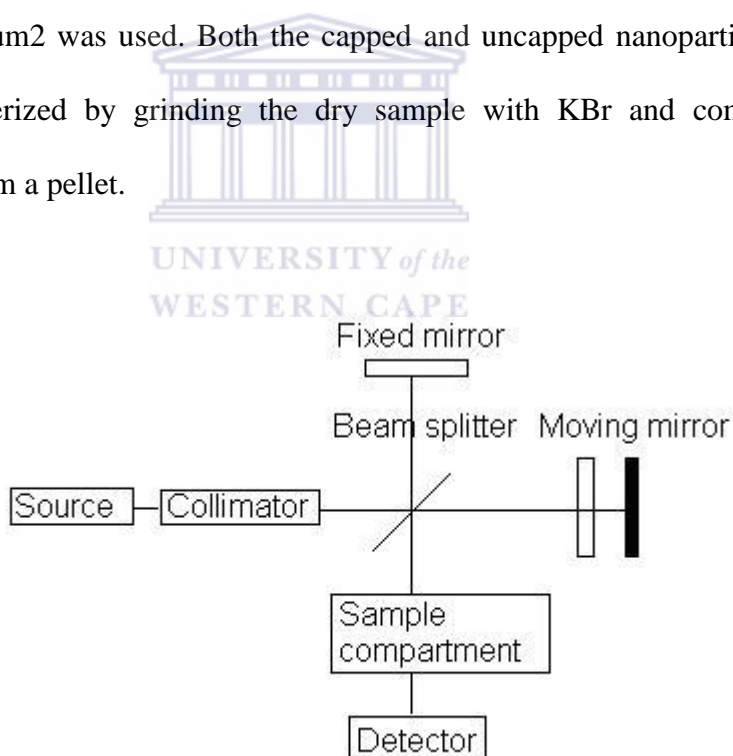
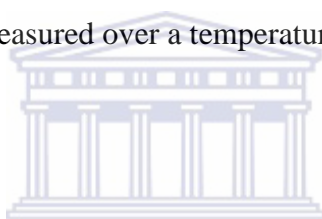


Figure 7: A basic schematic representation of the components of an IR spectroscopy instrument<sup>6</sup>.

### 3.3.5 TGA

Supporting data that proves the presence of the surfactant at the particle surface can be obtained from thermogravimetric analysis (TGA). In this analysis, a small amount of sample is placed in a crucible which is heated over a selected temperature range. As the temperature increases, volatile components within the sample will escape from the crucible, thus decreasing the mass <sup>7</sup>. A plot of weight percentage versus temperature reveals a curve showing progressive loss of mass as the temperature increases and can be used to determine what components of the sample were lost. A sample of 3-PPA and a sample of 3-PPA-capped  $Zn_{0.2}Fe_{2.8}O_4$  were analyzed with this technique using a Perkin Elmer TGA4000. The sample analysis was done under air and the decomposition measured over a temperature range of 30-900 °C.



### 3.3.6 Zeta Potential

Zeta potential measurements are based on the fact that colloidal particles possess a positive or negative electrostatic charge <sup>8</sup>. When an electric field is applied to the particle dispersion, the particles migrate in opposite directions depending on their charge with respect to the direction of the field. When the particles are irradiated in the process of migration they scatter light causing a Doppler shift which is dependent on the electrophoretic mobility shift of the colloids. The zeta potential calculation is based on the Smoluchowski equation which takes into account electrophoretic mobility, permittivity and viscosity of the colloid particles. The zeta potential of a sample can be determined by diluting a solvent with known properties (viscosity, dielectric constant and refractive index). The nanosizer is connected to a nanoplus (titrator) fitted with both acid and basic solution purposely to adjust the pH of the sample automatically. For this analysis, a NanoPlus AT titrator was used. A pH of 8

was selected for analysis of the zeta potential using 0.1 M solutions of sodium hydroxide (NaOH) and hydrochloric acid (HCl) as standards for adjusting the pH.

### 3.3.7 SQUID

Superconducting quantum interference device (SQUID) analysis is used to characterize the magnetic properties of a given material. The two main properties of superconductors, namely the Josephson effect and flux quantization are applied to measure small changes in the magnetic field of the superconductor while characterizing a sample <sup>9</sup>. The sample is placed into the instrument and exposed to a magnetic field that increases from negative to positive to yield the saturation magnetization ( $M_s$ ) of the sample (Fig. 8). This also reveals whether the material is ferromagnetic or paramagnetic depending on whether hysteresis is observed in the curves that are generated. Samples of  $Zn_xFe_{3-x}O_4$  ( $x = 0, 0.1, 0.2, 0.3, 0.4$ ) were characterized using a Quantum Design XL-7 SQUID Magnetometer (San Diego). The saturation magnetization was measured as a function of the magnetic field up to 30 000 Oe at 25 °C.

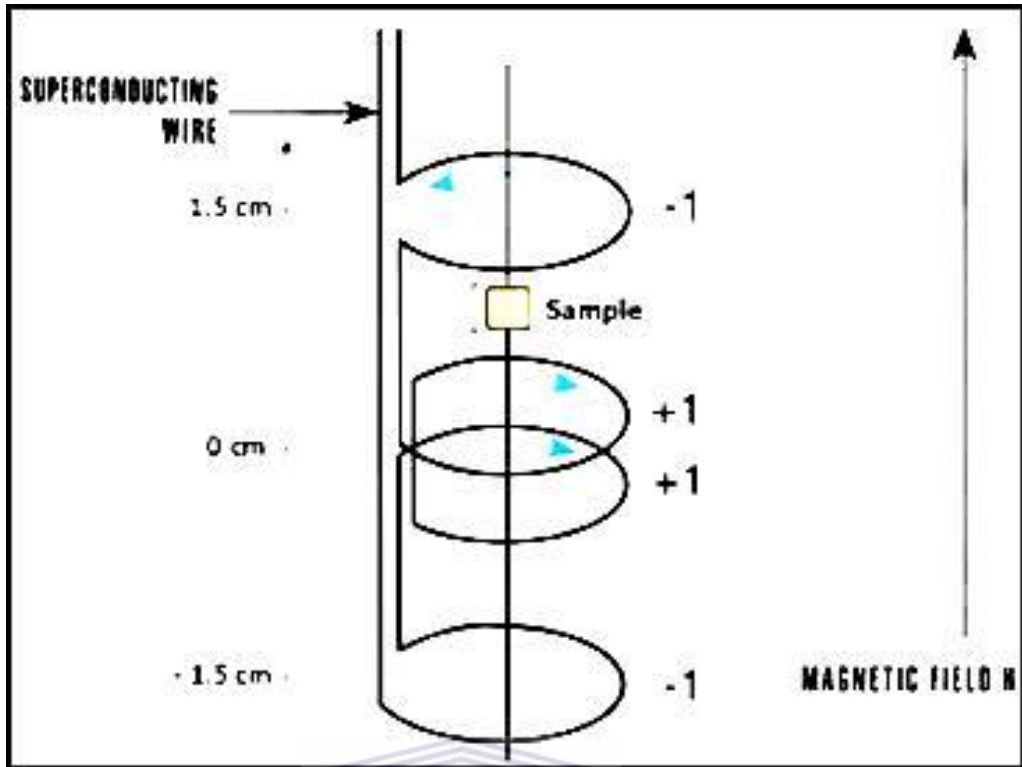
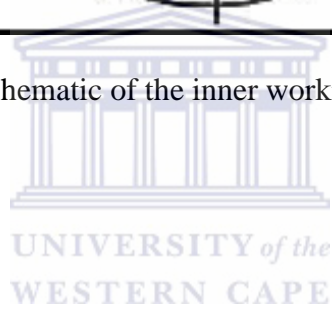


Figure 8: Basic schematic of the inner workings of a SQUID magnetometer.



### 3.4 References

1. TEM (Transmission Electron Microscopy) [Internet], <http://www.gitam.edu/eresource/nano/nanotechnology/tem.htm>. (Accessed 20 July 2015)
  2. A.L. Ryland, (1958) Journal of Chemical Education, **35**(2), 80-83.
  3. [Internet], [https://commons.wikimedia.org/wiki/File:Bragg\\_diffraction.pdf](https://commons.wikimedia.org/wiki/File:Bragg_diffraction.pdf). (Accessed 20 July 2015)
  4. [Internet], <http://www.seallabs.com/how-sem-eds-works.html>. (Accessed 30 July 2015)
  5. D.C. Harris, Quantitative Chemical Analysis, 6<sup>th</sup> Edition, (2003) New York : W.H. Freeman and Co., 485.
  6. How an FTIR Spectrometer Operates [Internet], [http://chemwiki.ucdavis.edu/Physical\\_Chemistry/Spectroscopy/Vibrational\\_Spectroscopy/Infrared\\_Spectroscopy/How\\_an\\_FTIR\\_Spectrometer\\_Operates](http://chemwiki.ucdavis.edu/Physical_Chemistry/Spectroscopy/Vibrational_Spectroscopy/Infrared_Spectroscopy/How_an_FTIR_Spectrometer_Operates). (Accessed 31 July 2015)
  7. PerkinElmer, A Beginner's Guide to Thermogravimetric Analysis, (2010), 3
  8. Particle Sciences Inc., (2012) Technical Brief 2.
- R. L. Fagaly, (2006) Review of Scientific Instruments, **77**, 101101-1 – 101101-45.

## Chapter 4

### Chapter Overview

Chapter 4 contains a brief discussion of the synthesis of undoped and doped zinc ferrite MNPs with emphasis on the results obtained from all the characterization techniques employed to analyse the NPs.

### 4. Results and Discussion

#### 4.1 Synthesis

Both the undoped and doped MNPs were successfully prepared in this research. Some product was lost due to magnetic attraction to the stirrer bar used during synthesis, but the amount lost is small enough to be negligible. Fig. 9 shows pure  $\text{Fe}_3\text{O}_4$  nanoparticles dispersed in deionized water. In Fig. 9.(a,b), and the nanoparticles from the same batch after exposure to a magnet. After being left for several minutes, the deionized water was completely clear as all the nanoparticles were attracted to the magnet. The same behaviour was observed for the doped nanoparticles tested in the same way (Fig. 9.(c,d)).

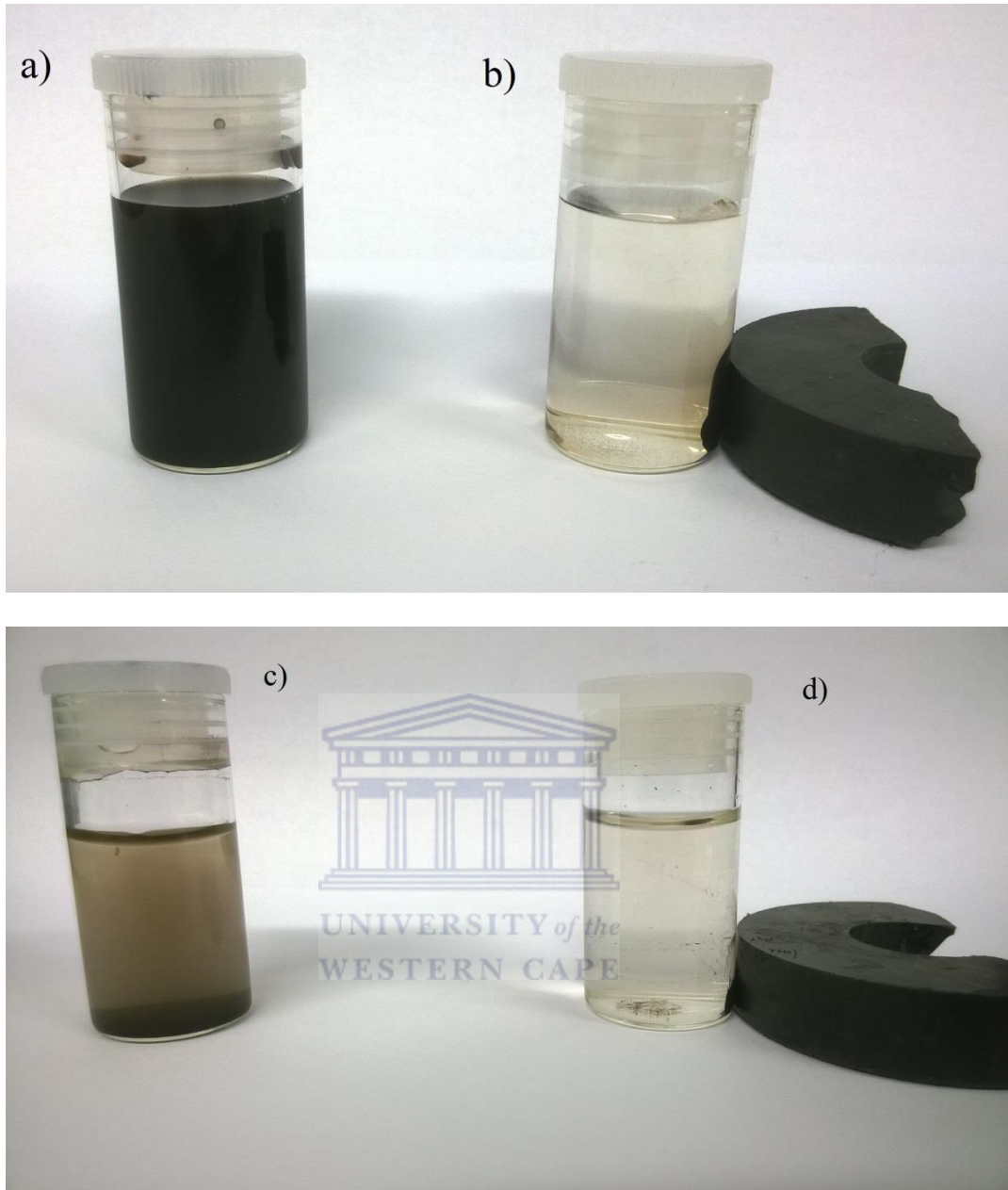


Figure 9: a) Pure iron oxide MNPs ( $x=0$ ) and c) doped MNPs ( $x=0.2$ ) suspended in deionized water. Attraction to an external magnetic field is seen in b) and d).

#### 4.2 HRTEM

Figure 10 shows micrographs obtained from the HRTEM characterization of uncapped iron oxide MNPs (Fig. 10.(a)) and MNPs capped with PEG (Fig. 10.(b)) synthesized in preliminary experiments. In both cases, the nanoparticles have spheroidal morphology. The lack of a capping agent is evident as the nanoparticles

appear highly agglomerated. The addition of PEG greatly improves the dispersion of the nanoparticles, as can be seen in Fig. 10.(b).

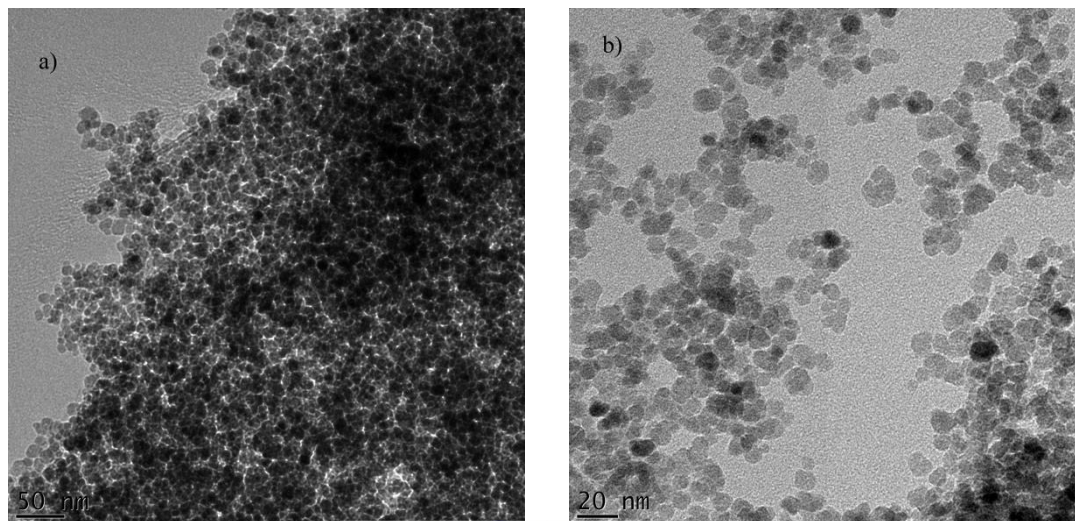


Figure 10: a)Uncapped iron oxide MNPs and b) PEG capped iron oxide MNPs synthesized in preliminary experiments.

Fig. 11 shows the HRTEM micrograms obtained from the characterization of the zinc-doped MNPs. The magnetic nanoparticles (MNPs) showed similar spheroidal morphology with and without the addition of the 3-PPA. The nanoparticles showed a high level of agglomeration without and with the inclusion of the 3-PPA surfactant. This could be due to an insufficient amount of surfactant relative to the amount of nanoparticles produced, and in turn, this led to challenges in estimating the particle size from the micrographs.

It was also seen that the presence of the zinc dopant had no visible effect on the morphology of the nanoparticles. This indicates that the dopant atoms assimilated easily within the crystal structure of the nanoparticles. Closer inspection of the MNPs showed the presence of lattice lines indicating high levels of crystallinity. This further proves that the zinc dopant was incorporated into the crystal structure

without causing physical irregularities. Estimation of particle sizes from HRTEM micrographs proved challenging due to the agglomeration of the nanoparticles. Fig 11.c) and 11.d) show particle sizes for  $Zn_{0.1}Fe_{2.9}O_4$  and  $Zn_{0.4}Fe_{2.6}O_4$  with average particle sizes of 10.23 nm and 9.26 nm respectively. These estimates are not completely reliable due to the agglomeration visible in micrographs, thus there is room for error in the particle size determination.

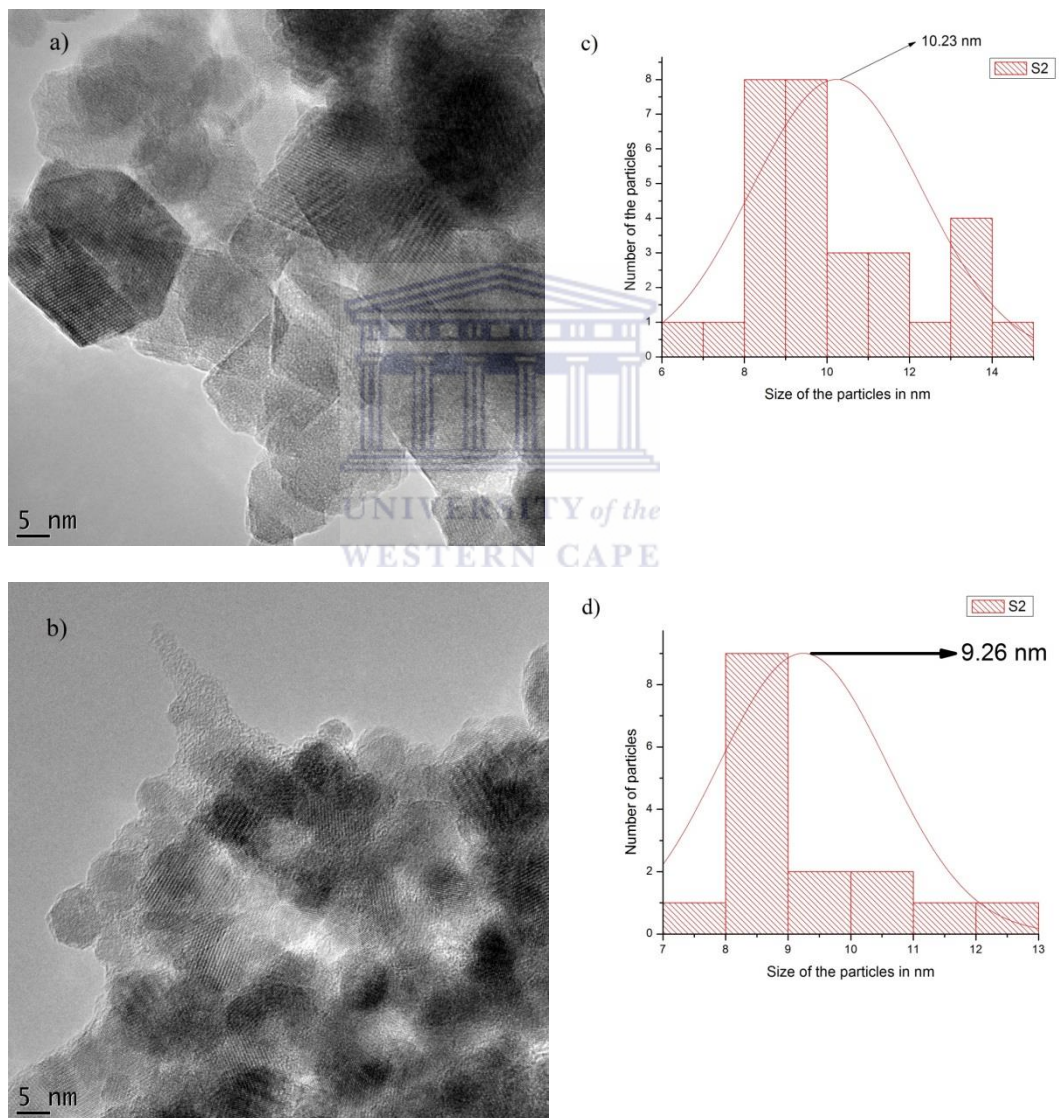


Figure 11: HRTEM micrographs of a) doped MNPs ( $x=0.1$ ), b) doped MNPs ( $x=0.4$ ) and their respective particle size distributions in c) and d).

### 4.3 XRD

The XRD spectra obtained for the undoped and doped MNPs is given in Fig. 12 below. The peaks that appeared were attributed to the crystal planes indexed at (220), (311), (400), (422), (511), and (440). This confirms the formation of the inverse spinel structure of magnetite. The peak indexed at (311) was used to estimate the average particle size for undoped and doped nanoparticles as can be seen in Tab. 1. by application of the Scherrer equation:

$$d_{(311)} = k\lambda/\beta\cos\theta \quad (4)$$

It was found that the particle sizes showed a slight increase in size as the amount of zinc dopant increased from  $x=0$  and reaching a maximum at  $x=0.2$ . Beyond this, the particle decreased through  $x=0.3$  and  $x=0.4$ . This could be due to the MNPs approaching a doping limit at  $x=0.2$  where the particle size and physicochemical properties reach a maximum value.

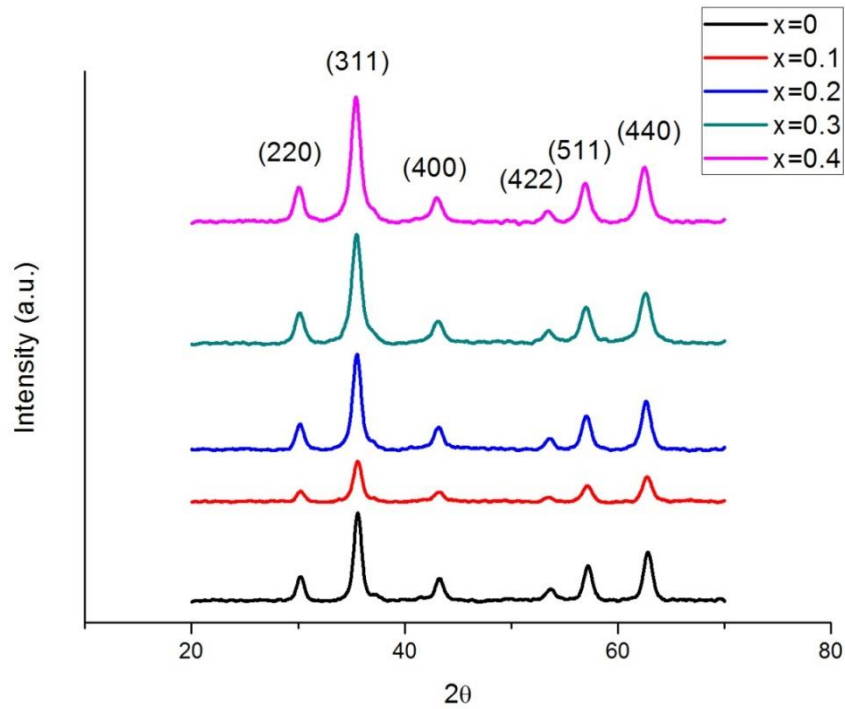


Figure 12: The XRD spectra for nanoparticles with the composition of  $Zn_xFe_{3-x}O_4$  ( $x = 0, 0.1, 0.2, 0.3, 0.4$ ).

Table 1: Particle size determined from XRD data and the Scherrer equation

	$2\theta$	$\theta$	radians	$\cos\theta$	$\lambda$ (nm)	FWHM	$\beta$	radians	$d_{(311)}$ (nm)
$x=0$	36.623	18.3115	0.3196	0.949361	0.154	1.7576	0.8788	0.01534	9.41
$x=0.1$	35.6504	17.8252	0.3111	0.951997	0.154	1.7302	0.8651	0.0151	9.52
$x=0.2$	35.5131	17.75655	0.3099	0.952364	0.154	1.5379	0.76895	0.01341	10.73
$x=0.3$	35.4857	17.74285	0.3096	0.952456	0.154	1.7027	0.85135	0.01486	9.68
$x=0.4$	35.4307	17.71535	0.3092	0.952577	0.154	1.7302	0.8651	0.0151	9.53

#### 4.4 FTIR

The spectra obtained from FTIR analysis can be seen in Fig. 4. In the spectrum of the uncapped nanoparticles (Fig. 4.(a)), the strong stretching band for the Fe-O within the nanoparticle crystal structure is visible at  $578\text{ cm}^{-1}$ . The broad stretching band for -OH bonds is observed at  $3394\text{ cm}^{-1}$  and is attributed to water molecules adsorbed to

the surface of the uncapped nanoparticles. The small peak at  $1619\text{ cm}^{-1}$  could be attributed to the C=O stretch of carbon dioxide within the instrument. The change in percentage transmittance was a good indication that capping with 3-PPA had taken place. The capped nanoparticles (Fig. 4.(b)) showed a similar Fe-O stretching band at  $588\text{ cm}^{-1}$ . The band observed at  $992\text{ cm}^{-1}$  and  $1103$  could be attributed to the stretching of P-O bonds. The small band observed at  $1391\text{ cm}^{-1}$  could be attributed to the bending of C-O-H while the band at  $1629\text{ cm}^{-1}$  could be attributed to the stretching frequencies of C=O in the carboxylate group. The broad band at  $3404\text{ cm}^{-1}$  could be attributed to the stretching band of O-H bonds in both the phosphate and carboxylate groups. Kalska-Szostko et al <sup>1</sup> reported the successful synthesis of iron oxide nanoparticles with 3-PPA as the surfactant, and their work was used to corroborate the findings of the FTIR analysis in this research. This shows that linkage of the 3-PPA to the nanoparticle takes place via the P=O in the phosphate group and iron atoms at the surface of the particle and that successful capping had been achieved.

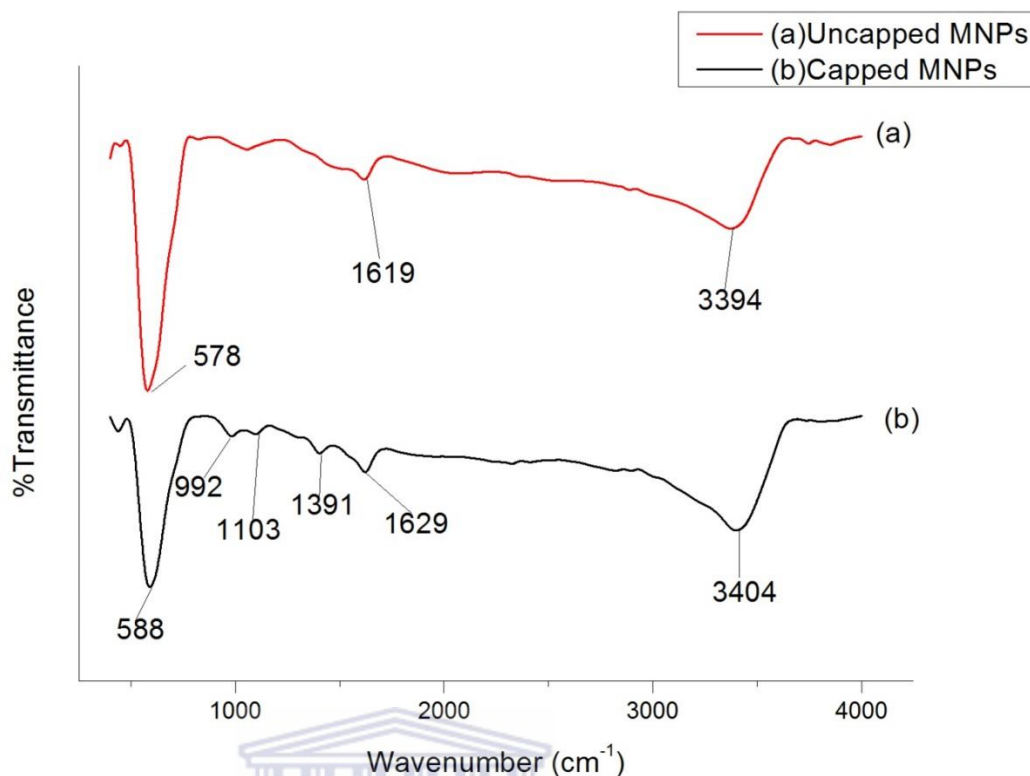


Figure 13: FTIR spectra of the (a) uncapped and (b) capped  $Zn_{0.2}Fe_{2.8}O_4$  nanoparticles.

#### 4.5 TGA

Fig. 14 shows the thermal decay of 3-PPA and 3-PPA capped zinc ferrite nanoparticles with  $x=0.2$ . For 3-PPA (Fig. 14.(a)) it is seen that from 30 °C to 156 °C there is an increase in mass. This is due to the hygroscopic nature of 3-PPA with water molecules accumulating in the sample while still at relatively low temperatures. From 156-900 °C a three-step decomposition can be seen. From 156 °C to approximately 375 °C there is a steep decrease in mass from 102% to 75%. This could be due to loss of the adsorbed water as well as the other components of the compound such as the phosphate ( $-PO(OH)_2$ ) group. The second loss of mass is observed from 375 °C to 540 °C which could be due to the loss of the carboxylate ( $-COOH$ ) group. The remnants of the 3-PPA resembled amorphous carbon. It is possible that this material might only decompose at temperatures beyond 900 °C.

The 3-PPA capped nanoparticle (Fig. 14.(b)) showed a very small decrease in mass, but this is due to the very small amount of 3-PPA bonded to the surface relative to the mass of the nanoparticles. The slow loss of mass from 30 °C to approximately 410 °C could be due to the slow release of the  $-PO(OH)_2$  group. The almost linear decrease which follows from 410 °C to 900 °C could be due to the loss of the carboxylate group. The differences between the two curves could be attributed to the nanoparticles having a catalytic effect on the thermal decomposition of the 3-PPA. Jurikova et al. reported the catalytic effect of iron oxide MNPs on the thermal decomposition of dextran, and it is likely that the same effect is being observed here<sup>2</sup>. This supports the FTIR analysis in confirming successful capping of 3-PPA onto the nanoparticles.

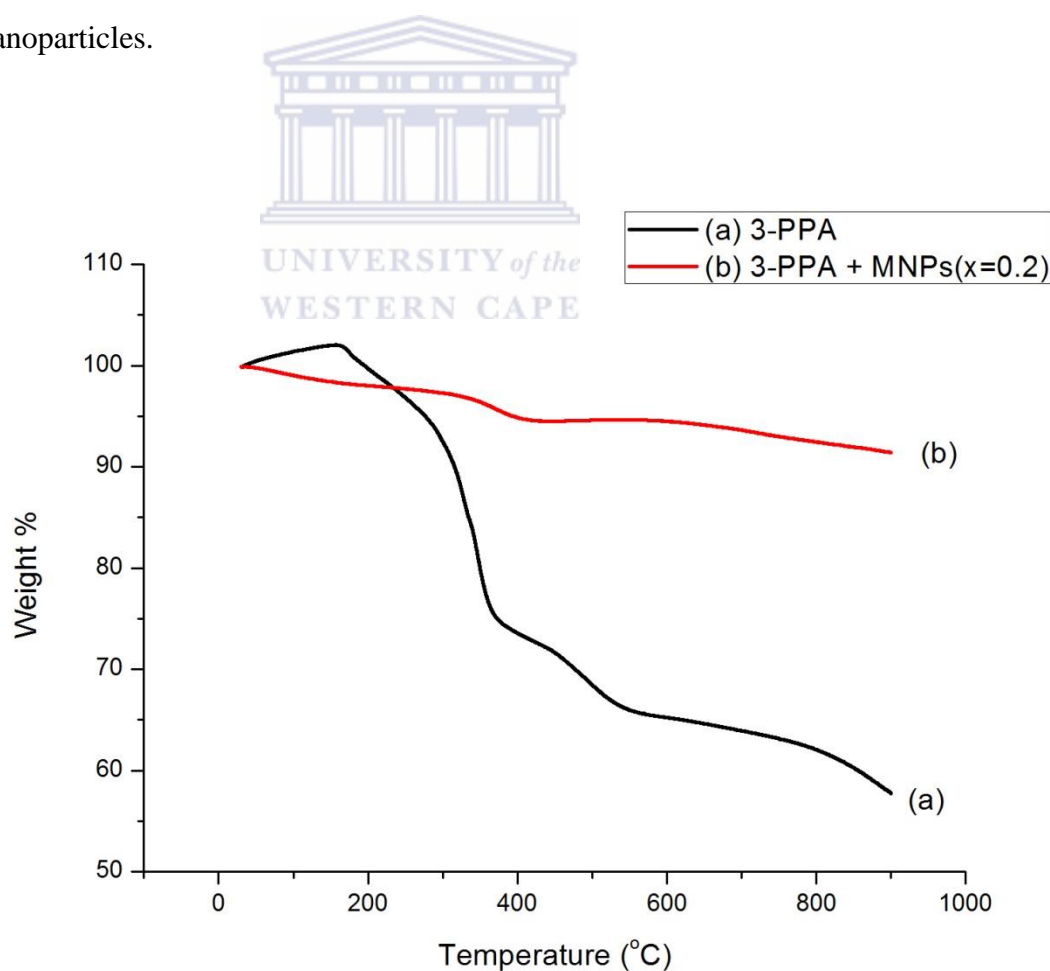


Figure 14: The thermal decomposition curves for (a) 3-PPA and (b) 3-PPA

#### 4.6 EDS

The EDS analysis was used to study elemental composition of the nanoparticles with results visible in Fig. 15(a,b). The spectra obtained for the undoped and uncapped MNPs indicated the presence of iron and oxygen with a percentage abundance of 42.03% and 20.02% respectively. The same test was performed on doped and capped MNPs. For  $x=0.2$  peaks for iron, oxygen and zinc were observed with percentage abundance of 12.33%, 24.94%, 0.97% respectively, while the presence of the phosphorous in the surfactant was not observed. For  $x=0.4$  peaks for iron, oxygen, zinc and phosphorous were observed with percentage abundance of 13.22%, 32.93%, 2.42% and 0.37% respectively. The peaks for copper and carbon that were observed were due to the grid onto which the samples were deposited for analysis and the carbon support structure which forms part of the grid. From this data it can be seen that the percentage abundance is not in agreement with the formulae of the respective MNPs. This inconsistency, along with the absence of peaks for phosphorous for MNPs with  $x=0.2$  could be affected by factors such as non-homogeneity within the reaction mixture as well as the effect of size differences in the particles onto which the instrument had focused to capture the micrograph. The agglomeration of the MNPs visible in the images could also cause inconsistencies in the elemental analysis. However, since this technique only yields data on a very small area of the sample, it cannot be assumed that the obtained percentage abundance is applicable to the entire sample.

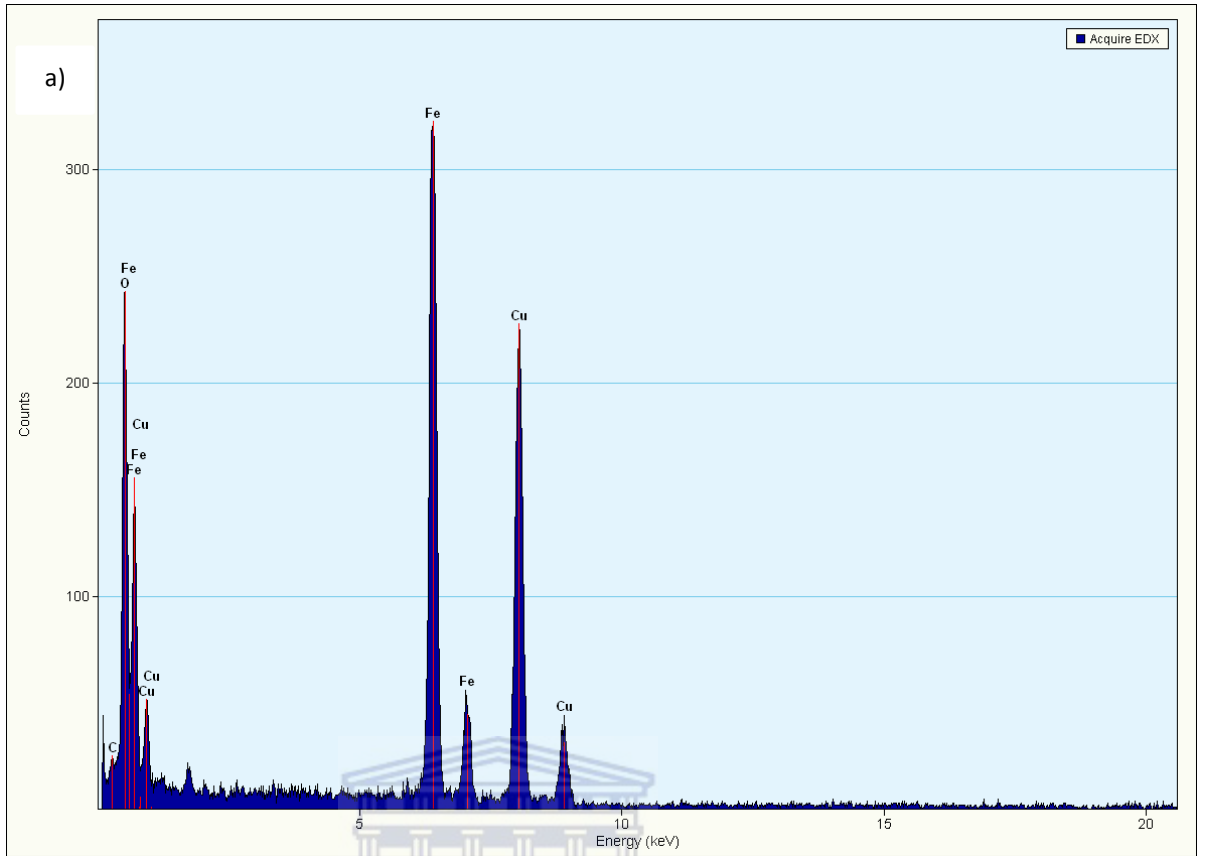


Figure 15a): EDS spectrum of  $Zn_{0.1}Fe_{2.9}O_4$  MNPs

UNIVERSITY of the  
WESTERN CAPE

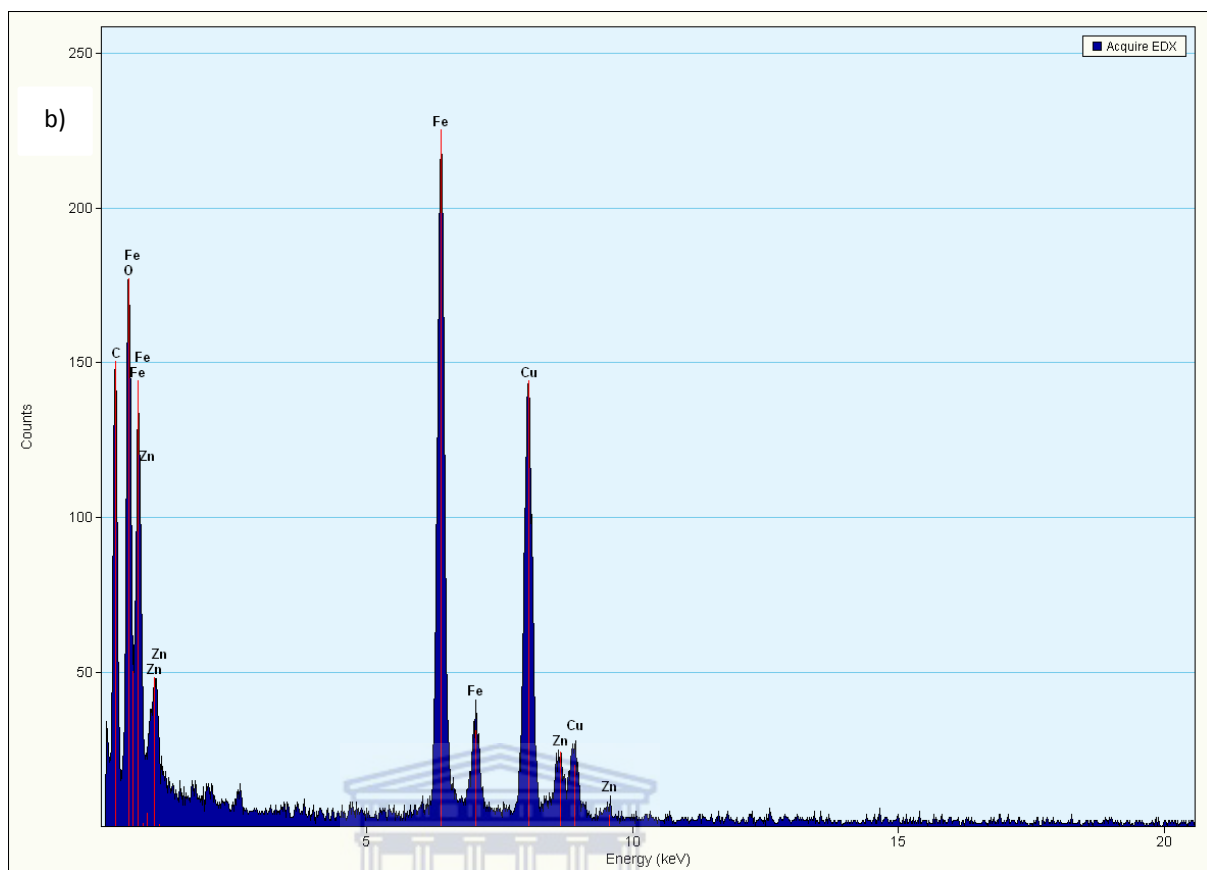


Figure 15b): EDS spectrum of  $Zn_{0.4}Fe_{2.6}O_4$

UNIVERSITY of the  
WESTERN CAPE

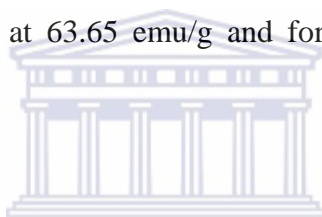
#### 4.7 Zeta Potential

Zeta potential measurements were made to analyse the surface charge of the MNPs. A pH of 8 was selected for analysis. Uncapped iron oxide MNPs ( $x=0$ ), as well as iron oxide MNPs ( $x=0$ ) and doped MNPs ( $x=0.2$ ) capped with 3-PPA were characterized with this technique, and the zeta potentials obtained were 0.32 mV, -0.87mV and -0.076 mV respectively. At low pH values, iron oxide MNPs are reported to have a negative zeta potential in water<sup>3</sup>. The positive value obtained for the uncapped iron oxide MNPs ( $x=0$ ) could be due to localized inhomogeneity within the solvent after pH adjustment by the instrument. A positive zeta potential in a basic environment is not common and requires further investigation. The negative values measured for the remaining two samples confirm successful capping with 3-

PPA and are brought about by the ionization of  $-C=O$  to  $-C-O^-$  in the carboxyl group.

#### 4.8 SQUID

The saturation magnetization ( $M_s$ ) for  $Zn_xFe_{3-x}O_4$  ( $x = 0, 0.1, 0.2, 0.3, 0.4$ ) was characterized using SQUID analysis with the magnetization curves shown in Fig. 16. The lack of hysteresis loops in the curves for all the five samples indicates that superparamagnetic behaviour is inherent at all doping levels ( $x=0$  to  $x=0.4$ ). At  $x=0$  the nanoparticles exhibit saturation of 68.50 emu/g. The value of  $M_s$  observed for  $x=0.1$  and  $x=0.2$  were 72.08 emu/g and 73.37 emu/g respectively. For  $x=0.3$  saturation was observed at 63.65 emu/g and for  $x=0.4$  saturation was reached at 66.32 emu/g.



Results reported by Liu et al.<sup>4</sup> show a similar trend in which the saturation magnetization increased from  $x=0$ , starting at 52.34 emu/g and reached a maximum at  $x=0.2$  with a value of 80.93 emu/g, followed by a decrease as the  $x$  values increased. At  $x=0.4$  the saturation magnetization had decreased below the 43.14 emu/g. In comparison, the trend observed in Fig. 16 deviates at  $x=0.4$  where the saturation increased instead of exhibiting a further decrease. An important observation is made when the  $M_s$  values from Fig. 16 are compared to the particle sizes determined by the Scherrer equation as seen in Table 1. The saturation magnetization and particle size increase from  $x=0$  to  $x=0.2$ , followed by a consistent decrease in particle size, with the exception of the increased magnetization at  $x=0.4$ . The maximum reached at  $x=0.2$  was expected, based on the work of Liu et al., and confirms that  $x=0.2$  is the doping limit for zinc ferrite nanoparticles. The deviation

from the relation observed in particle size and saturation magnetization at  $x=0.4$  could be due improved distribution of the Zn(II) cations within the crystal structure in comparison to doping at  $x=0.3$ . During synthesis, there is no control over the placement of dopant ions within the crystal structure, only the dopant concentration. However, consistency in this trend requires further investigation. The saturation magnetizations of the nanoparticles presented in this work were higher than that for the reported value of pure iron oxide MNPs. At  $x=0$ , the value is higher than the reported value of 50 emu/g <sup>5</sup>, highlighting the effectiveness of the synthetic procedure. It is possible that higher values can be obtained if the ripening period is extended, since higher saturation was reported by Liu et al, especially at  $x=0.2$ . The improved magnetic properties obtained from doping could lead to more efficient and fast acting biomedical systems in which MNPs are used.

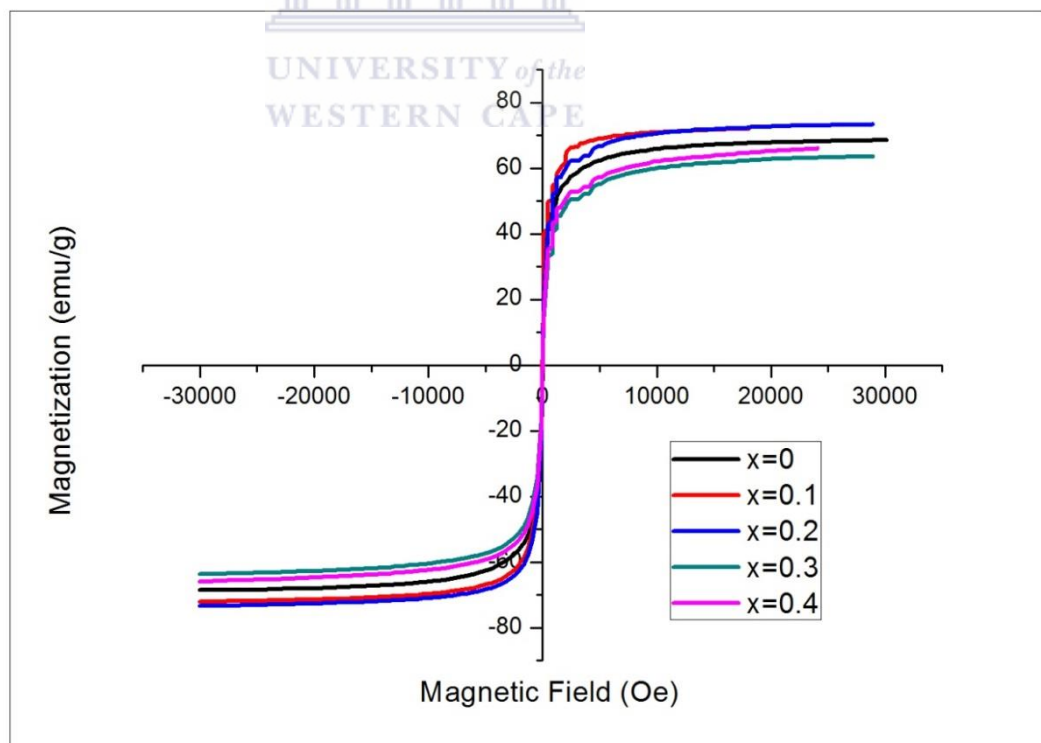


Figure 16: Field-dependent magnetization at room temperature of  $Zn_xFe_{3-x}O_4$  for increasing amounts of zinc.

#### 4.9 References

1. B. Kalska-Szostko, M. Rogowska, D. Satuła, (2013) *Colloids and Surfaces B: Biointerfaces*, **111**, 656– 662.
2. A. Jurikova, K. Csach, J. Miskuf, M. Koneracka, V. Zavisova, M. Kubovcikova, P. Kopcansky, (2012) *Acta Physica Polonica A*, **121**, 1296-1298.
3. A. L. Andrade, D. M. Souza, M. C. Pereira, J. D. Fabris, R. Z. Domingues, (2009) *Cerâmica* **55**, 420-424.
4. J. Liu, Y. Bin, and M. Matsuo, (2012) *Journal of Physical Chemistry C*, **116**, 134–143.
5. Q. Song, Z.J. Zhang, (2006) *Journal of Physical Chemistry B*, **110**, 11205–11209.



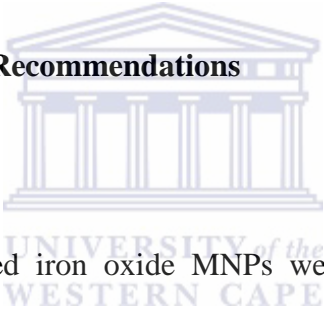
## Chapter 5

### Chapter Overview

In this chapter, conclusions are made based on the experimental data discussed in Chapter 4, followed by future work and recommendations.

### 5. Conclusion and Recommendations

#### 5.1 Conclusions



In conclusion, zinc-doped iron oxide MNPs were successfully prepared via co-precipitation. This route was a one-pot synthetic approach in which an aqueous solution of both ferric and ferrous salts with zinc as the dopant and 3-PPA as the surfactant was used to prepare iron oxide MNPs. The effects of the zinc doping on the physical and chemical properties of the nanoparticles was then investigated. Analysis with HRTEM and XRD showed that particles of between approximately 9.5 and 10.5 nm in size were obtained. The enhancement of the saturation magnetization and the relation to particle size were observed upon doping with zinc. The  $M_s$  value of 73.3 emu/g and maximum size of approximately 10.5 nm observed at the doping level  $x=0.2$  leads to the conclusion that this is the doping limit for zinc ferrite. Capping with 3-PPA was confirmed with FTIR, TGA and zeta potential, but little change was observed in the agglomeration of the nanoparticles with or without

the surfactant. Some work remains to fully improve the MNP system described in this work, but the data collected so far indicates that these nanoparticles have great potential for application in the diagnosis and/or treatment of breast cancer.

## **5.2 Recommendations**

Synthesis via the co-precipitation route opens up multiple routes for further investigation. The following work is proposed for further investigation:

- Varying the pH during synthesis
- Varying surfactant concentration
- Varying reaction temperature
- Characterization of the elemental composition using inductively-coupled plasma optical emission spectroscopy (ICP-OES)
- Bioconjugation with a known anti-body and/or drug for the targeting and/or treatment of breast cancer
- Separation of breast cancer cells using bioconjugated MNPs
- Repeat of the separation study using zinc-doped MNPs
- Validation of the separated cells to confirm successful targeting and separation by MNPs